RESEARCH ARTICLE

BIOENGINEERING &
TRANSLATIONAL MEDICINE

Unique osteogenic profile of bone marrow stem cells stimulated in perfusion bioreactor is Rho-ROCK-mediated contractility dependent

Shuntaro Yamada[1] 🖻 | Mohammed A. Yassin[1] | Francesco Torelli[1] |
Jan Hansmann[2,3,4] | Jeremy B. A. Green[5] | Thomas Schwarz[2] | Kamal Mustafa[1]

[1]Center of Translational Oral Research (TOR)-Tissue Engineering Group, Department of Clinical Dentistry, Faculty of Medicine, University of Bergen, Norway

[2]Translational Center Regenerative Therapies, Fraunhofer Institute for Silicate Research ISC, Würzburg, Germany

[3]Chair of Tissue Engineering and Regenerative Medicine, University Hospital Würzburg, Würzburg, Germany

[4]Department of Electrical Engineering, University of Applied Sciences Würzburg-Schweinfurt, Schweinfurt, Germany

[5]Centre for Craniofacial & Regenerative Biology, Faculty of Dentistry, Oral & Craniofacial Sciences, King's College London, UK

Correspondence
Kamal Mustafa, Center of Translational Oral Research (TOR)-Tissue Engineering Group, Department of Clinical Dentistry, Faculty of Medicine, University of Bergen, Årstadveien 19, 5009 Bergen, Norway.
Email: kamal.mustafa@uib.no

Abstract

The fate determination of bone marrow mesenchymal stem/stromal cells (BMSC) is tightly regulated by mechanical cues, including fluid shear stress. Knowledge of mechanobiology in 2D culture has allowed researchers in bone tissue engineering to develop 3D dynamic culture systems with the potential for clinical translation in which the fate and growth of BMSC are mechanically controlled. However, due to the complexity of 3D dynamic cell culture compared to the 2D counterpart, the mechanisms of cell regulation in the dynamic environment remain relatively undescribed. In the present study, we analyzed the cytoskeletal modulation and osteogenic profiles of BMSC under fluid stimuli in a 3D culture condition using a perfusion bioreactor. BMSC subjected to fluid shear stress (mean 1.56 mPa) showed increased actomyosin contractility, accompanied by the upregulation of mechanoreceptors, focal adhesions, and Rho GTPase-mediated signaling molecules. Osteogenic gene expression profiling revealed that fluid shear stress promoted the expression of osteogenic markers differently from chemically induced osteogenesis. Osteogenic marker mRNA expression, type 1 collagen formation, ALP activity, and mineralization were promoted in the dynamic condition, even in the absence of chemical supplementation. The inhibition of cell contractility under flow by Rhosin chloride, Y27632, MLCK inhibitor peptide-18, or Blebbistatin revealed that actomyosin contractility was required for maintaining the proliferative status and mechanically induced osteogenic differentiation in the dynamic culture. The study highlights the cytoskeletal response and unique osteogenic profile of BMSC in this type of dynamic cell culture, stepping toward the clinical translation of mechanically stimulated BMSC for bone regeneration.

KEYWORDS
actomyosin contraction, bioreactor, bone tissue engineering, fluid shear stress, osteogenic differentiation, Rho GTPase signaling

1 | INTRODUCTION

The fate and growth of bone marrow mesenchymal stem/stromal cells (BMSC) are tightly regulated by mechano-environmental factors.[1,2] The forces of load and torsion applied to bone are converted to shear forces by altered interstitial fluid flow in bone marrow, which is exerted on the resident cells, including mechanosensitive BMSC.[3] For example, hydrostatic pressure, fluid shear stress, and altered rheological properties of BMSC niche regulate their fate into osteoblast, adipocyte, chondrocyte, or stromal cell, balancing bone homeostasis and remodeling.[3,4] Physical activity increases fluid shear stress in bone marrow, which promotes bone remodeling by energizing osteoblasts and their progenitors, whereas a disbalanced mechano-environment by physiopathological conditions such as aging, diseases (i.e., osteoporosis), and disuse favors adipogenesis.[3,5–9]

The osteogenic nature of BMSC under fluid shear and its plausible mechanism have been predominantly described by conventional monolayer cell culture experiments. In osteoinductive medium (i.e., in the presence of dexamethasone, beta-glycerophosphate, and ascorbic acid), BMSC preferably respond to fluid shear stress as small as 0.01 Pa up to 2 Pa by upregulating osteogenic markers such as Runt-related transcription factor 2 (Runx2), Osteopontin (Opn), Bone morphogenetic protein 2 (Bmp2), alkaline phosphatase (ALP), collagen type 1 (Col1), and Osteocalcin (Ocn) accompanied by increased mineralization and extracellular matrix formation.[10-19] BMSC subjected to fluid flow undergo dynamic cytoskeletal rearrangement moderated by integrins, focal adhesion, MAPK/ERK signaling, Rho- and Hippo-YAP/TAZ signaling, which are tightly linked to osteogenic differentiation.[10,12,13,20–22] The evidence of flow-induced osteogenic differentiation in the absence of the osteoinductive medium is rather limited. Approximately 1 Pa shear stress was reported to increase the enzymic activity of ALP and the expression of osterix (Osx), Opn, and Col1, but whether these cellular responses can be considered as osteogenic differentiation is debatable.[21,23,24]

The knowledge gained from the field of mechanobiology has been transferred into tissue engineering for bone regeneration where three-dimensional (3D) scaffolds are combined with BMSC to create transplantable constructs. With 3D scaffolds, gas, nutrient, and waste transport to/from the loaded cells has mostly relied on passive diffusion in static culture, causing the heterogeneity of cell growth and regenerative capacity.[25,26] Therefore, high expectations have been placed on the use of perfusion bioreactor systems to improve cell production. The rationale of applying bioreactors in bone tissue engineering is threefold: to uniform nutrient and gas distribution within 3D constructs to ensure the homogeneity of cell distribution and their functionality among the constructs, to mimic the mechanical environment of bone and bone marrow to stimulate osteogenic properties of the cells, and to automate cell production process to reduce the risk of human-error and improve cost-effectiveness.[27] Similar to the 2D observations, studies using the various prototypes of bioreactors, mostly in the presence of the osteoinductive medium, reported the preferable effects of 3D perfusion culture on osteogenic differentiation.[28–35] Notably, the concept was proven by a study that

BMSC co-cultured with vascular endothelial cells in the osteoinductive medium that was preconditioned in a perfusion bioreactor improved bone formation and visualization after transplantation into calvaria bone defects.[29] We previously reported that the osteogenesis of BMSC could be induced mechanically by the sub-physiological level of flow, even in the absence of the osteoinductive medium, showing the upregulated expression of osteogenic markers and the improved functionality of the cells including matrix formation and mineralization in a perfusion bioreactor.[36] Interestingly, BMSC in a 3D environment are reportedly more perceptive to shear stress than that in a 2D environment, but the cellular mechanisms of mechanically stimulated osteogenesis in a 3D dynamic culture remain underdocumented.[37] To translate the technology into clinical application, in depth understanding of cellular response is necessary. Therefore, in the present study, we aimed at elucidating mechanically induced osteogenesis by fluid flow on 3D porous scaffolds by focusing on signaling in cytoskeletal rearrangement and osteogenic profiling in depth. The dynamic cell culture was performed using a custom-designed bioreactor with experimental parameters disclosed, and flow characteristics was computationally estimated to correlate the magnitude of shear stress with cellular behaviors.

2 | MATERIALS AND METHODS

2.1 | BMSC isolation and cell culture

The study was approved by the Norwegian Animal Research Authority (local approval number 20146866) and conducted according to the European Convention for the Protection of Vertebrates used for scientific purposes. BMSC were isolated from femurs of male Lewis rats euthanized by lethal doses of carbon dioxide and cervical dislocation. The cells were maintained for both static and dynamic culture in α-minimum essential medium (α-MEM: 22571; Gibco™, USA) supplemented with 1% penicillin and streptomycin (SV30010; HyClone, USA) and 10% fetal bovine serum (FBS: 10270-106; Gibco™, USA) at 37°C in 5% CO_2. The expression of putative stem cell markers and the capacity of multilineage differentiation were previously verified.[36] BMSC from the third to fifth passages were used in the study. Osteoinductive medium (OM) used as a positive control for osteogenic differentiation consisted of α-MEM supplemented with 1% penicillin and streptomycin, 10% FBS, 10 nM dexamethasone (D4902; Sigma, USA), 10 mM beta-glycerophosphate (G9422; Sigma, USA), and 173 μM L-ascorbic acid (A8960; Sigma, USA).

2.2 | Preparation of 3D porous scaffolds of poly (L-lactide-co-trimethylene carbonate)

3D porous scaffolds with a diameter of 12 mm and a thickness of 1.2 mm were fabricated by a solvent-casting/salt-leaching technique as described previously.[38] Briefly, synthetic polymers, poly(L-lactide-co-trimethylene carbonate) 70:30 (RESOMER® LT
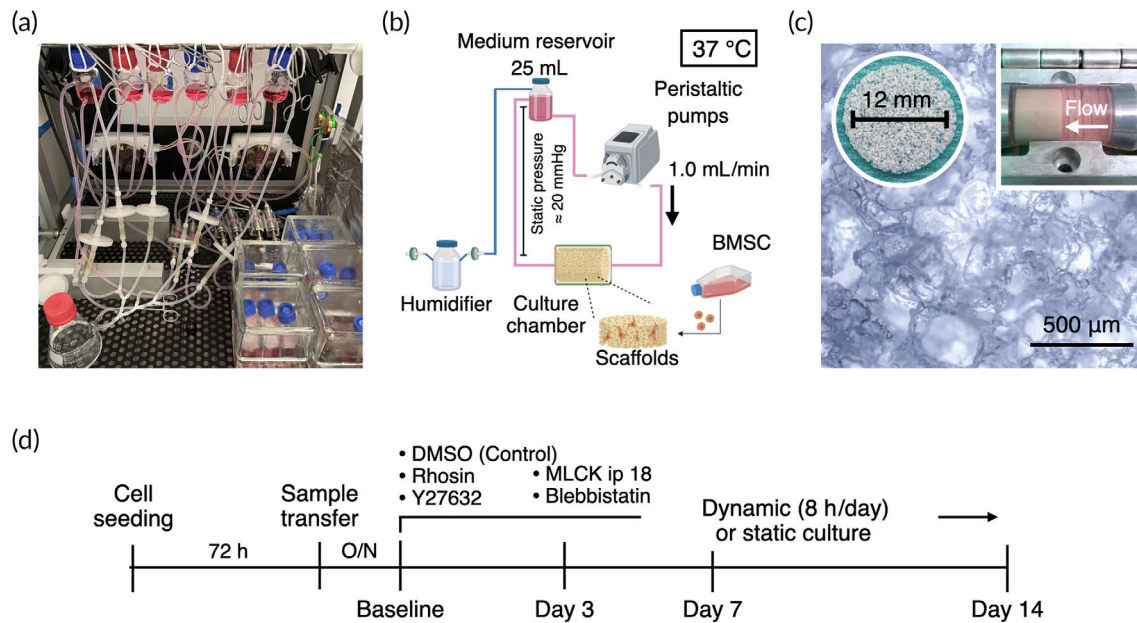
FIGURE 1 Experimental design and perfusion bioreactor. (a) The bioreactor used for 3D dynamic culture in the present study consists of integrated incubator and perfusion systems. (b) Schematic illustration of experimental setting including environmental factors in the dynamic cell culture. (c) Five cell-laden porous scaffolds of poly(L-lactide-co-trimethylene carbonate) were placed in the sample chambers where 25 mL of growth medium was perfused at 1.0 mL/min. (d) Experimental timeline.

706S; Evonik, Germany), were dissolved in chloroform and mixed with sodium chloride (NaCl) at a weight ratio of 1:10. After the slow evaporation of chloroform, the scaffolds were thoroughly washed to remove NaCl particles. Scaffolds were sterilized by 75% ethanol and UV irradiation prior to cell seeding. A total of 250,000 cells were seeded per scaffold in 48 well plates.

2.3 | Bioreactor system and 3D dynamic cell culture under perfusion

A custom-designed GMP-complied laminar flow perfusion bioreactor was utilized in the study. It consisted of an integrated incubator system with environmental sensors (i.e., temperature, gas concentration, pressure: details previously described[39]) and peristaltic pumps (Figure 1a). In the bioreactor, 25 mL of the growth medium was perfused, and the medium was refreshed twice a week unless otherwise mentioned (Figure 1b). The medium reservoirs were connected to ventilation filters via humidifiers to allow for gas exchange while minimizing medium evaporation. Approximately 20 mmHg of hydrostatic pressure was applied to sample chambers where five cell-laden scaffolds were placed in order to prevent air bubble formation during the dynamic cell culture (Figure 1c). Optimal flow rate for the cells was preliminarily determined at 1.0 mL/min.[39]

The experimental flow was given in Figure 1d. Briefly, 72 h after cell seeding on the scaffolds, five cell-laden scaffolds were transferred into the sample chamber in the bioreactor. The following day was defined as the baseline when dynamic cell culture has begun. Dynamic cell culture continued for 8 h a day for 14 days. As a control, five cell-

laden scaffolds were stacked and placed in a flask with 25 mL medium in the incubator space of the bioreactor to equalize the cell-to-medium ratio and environmental fluctuation. The samples were collected on Days 3, 7, and 14 for analyses, and the experiment was independently repeated three times unless otherwise mentioned.

2.4 | Computational fluid dynamics simulation

For flow characterization during dynamic cell culture, an in silico modeling was performed as previously described.[39] Briefly, the geometry of the scaffolds was obtained by microcomputed tomography (microCT: SkyScan 1172;Bruker-MicroCT, Kontich, Belgium) using 40 kV and 250 mA at 10 μm spatial resolution. The geometry was then imported in .stl file as a solid object using COMSOL Multiphysics version 6.0 (COMSOL AB, Sweden). Scaffold geometries were placed in a digitally reproduced sample chamber. From the inlet, fully developed flow of 1.0 mL/min was prescribed. At the outlet, pressure at 8.6 Pa was prescribed as a boundary condition, which was defined based on pressure drop over the scaffolds in a macro model as previously proposed.[39,40] Incompressible Newtonian fluid (described by Navier–Stokes equations) with a dynamic viscosity of 0.6922 mPa*s and density of 993.37 kg/m^3 was defined, which was governed by the Navier–Stokes equation and the continuity equation as follows:

$$\rho(u.\nabla)u = \nabla.[-pI + K] + F$$

$$\rho\nabla.u = 0$$

$$K = \mu\left(\nabla u + (\nabla u)^T\right)$$

where ρ, u, ∇, p, I, K, F, and μ are the fluid density, the fluid velocity, the divergence operator, the pressure, the identity tensor, the stress tensor, the body force per unit volume, and the dynamic viscosity of the fluid, respectively.

Nonslip boundary conditions were implemented at the solid walls.

2.5 | Pharmacological modulation of actomyosin contractility

To investigate the role of cytoskeletal rearrangement in BMSC growth and differentiation under flow, four inhibitors and two enhancers of actomyosin contractility were applied.

For the inhibition, 20 μM Rhosin chloride (Rhosin: 5003; Biotechne, UK), 10 μM Y27632 dihydrochloride (Y27632: 1254; Biotechne, UK), 1 μM MLCK inhibitor peptide 18 (MLCK ip 18: HY-P1029; MedChemExpress, USA), or 10 μM Blebbistatin (203390; Sigma-Aldrich, USA) was added to the culture medium during the dynamic cell culture to inhibit Rho GTPase, Rho-associated coiled-coil containing protein kinase (ROCK), myosin light chain kinase (MLCK), and myosin II, respectively (Figure S1A). The optimal concentrations of each inhibitor were determined preliminarily as the concentrations that mitigated actomyosin contractility without deteriorating cell viability and growth for 14 days (Figure S1). It was also confirmed that these inhibitors did not significantly influence on Runx2 expression in the static condition without the osteoinductive stimuli. Narciclasine (Narc: HY-16563; MedChemExpress, USA) and Calyculin A (CalA: sc-24000; Santa Cruz Biotechnology, USA) were used to activate Rho-ROCK signaling and to induce actomyosin contraction via the inhibition of myosin light chain phosphatase, respectively (Figure S2A,B). Dimethyl sulfoxide (DMSO) was used as a solvent and acted as a control. The culture media with inhibitors were refreshed every 2 days for 14 days.

2.6 | Reverse transcription-quantitative polymerase chain reaction and gene expression array

Samples for gene expression assay were collected on Days 7 and 14. After being immediately snap-frozen in liquid nitrogen, the samples were stored at −80°C. Total RNA was extracted using a Maxwell® 16 Cell LEV Total RNA Purification Kit (AS1280; Promega, USA) in accordance with the manufacturer's protocol. Reverse transcription was undertaken using a High-Capacity cDNA reverse Transcription Kit (4368813; Applied Biosystems, USA). RT-qPCR was performed with the StepOne™ real-time PCR system (4376357; Applied Biosystems) with TaqMan® Universal Master Mix (4352042; Applied Biosystems). The amplification was performed as follows: initial activation of polymerase at 95°C for 20 s followed by 40 cycles of PCR, at 95°C for 1 s (denature) and 60°C for 20 s (anneal and extend).

The tailored panels of gene expression assay for cytoskeletal rearrangement and osteogenesis were designed with reference to the predetermined TaqMan® gene expression arrays for focal adhesion (4413255-RPMFWWX; Applied Biosystems), cytoskeleton regulators (4413255-RPPRJ2T; Applied Biosystems), and osteogenesis (4413255-RPZTD3T; Applied Biosystems). A set of primers used in the study is listed in Tables S1–S3. Relative expression of each mRNA was calculated with the ΔΔCt method.[41]

2.7 | Gene set enrichment analysis

A list of differentially expressed genes (DEGs) identified through statistical analysis was further analyzed using the R package gprofiler2 and the STRING database version 11.5. Functional enrichment of the DEGs was evaluated using the open-source software Cytoscape version 3.9.1 by referencing the Reactome Pathways and UniProt databases.

2.8 | Cytoskeleton antibody microarray

To capture the overview of cytoskeletal rearrangement, ELISA-based antibody microarray was performed using Cytoskeleton Array kit (PCP141; Full Moon BioSystem, USA) according to the manufacturer's protocol. Briefly, samples were collected on Day 3, and protein extraction was performed by vigorous vortexing with lysis beads in the extraction buffer. Due to low protein yield, cell lysate obtained from three independent experiments was pooled. The protein samples were labeled in biotin dissolved in dimethylformamide in the labeling buffer. The biotinylated samples were then incubated with the antibody microarray slides followed by detection with Cy3-Streptavidin solution. The slides were scanned by a GenePix® Microarray Scanner (Molecular Devices, USA) and quantified using GenePix® ProMicroarray Image Analysis Software.

2.9 | ROCK enzymic activity assay

The enzymic activity of ROCK was measured on Days 3 and 7 by using ROCK Activity Assay Kit (ab211175; Abcam, USA) according to the manufacturer's protocol. Cell lysate was obtained in mammalian cell lysis buffer (ab179835; Abcam) with protease and phosphatase inhibitor cocktail (ab201119; Abcam). The cell lysate was added to wells where myosin phosphate target subunit 1 (MYPT1) was coated. Kinase reaction was initiated by adding 10 mM dithiothreitol (DTT) and 2 mM adenosine triphosphate (ATP). The wells were then incubated for 60 min at room temperature to phosphorylate MYPT1. Subsequently, the wells were incubated with anti-phospho-MYPT1 (Thr696) for 60 min at room temperature followed by secondary incubation with HRP-conjugated antibody for another 60 min at room temperature. The optical density of the HRP substrates was measured at 450 nm using a Varioskan™ LUX multimode microplate reader (VLBL00D0; Thermo Scientific, Finland).

2.10 | Immunofluorescence and confocal microscopy

For immunofluorescence, samples were fixed in 4% paraformaldehyde (PFA) for 15 min at room temperature except for collagen staining. To detect phosphorylated proteins, fixation was undertaken in the presence of protease and phosphatase inhibitor (ab201119; Abcam, UK). The samples were then permeabilized in 0.1% Triton X-100 in PBS for 15 min at room temperature. For collagen staining, samples were fixed and permeabilized in ice-cold methanol for 5 min at $-20°C$. The samples were then incubated in a blocking buffer consisting of 10% normal goat serum (NGS: ab7481; Abcam, USA) in 0.1% Tween-20 in PBS (PBSTw) for 60 min at room temperature. After blocking, the samples were incubated with the following primary antibodies in PBSTw at 4°C overnight: rabbit anti-non-muscle myosin 2A antibody (NM2A: 1:200, 909801; BioLegend, USA), mouse anti-non-muscle myosin 2B antibody (NM2B: 1:200, GTX634160; GeneTex, USA), mouse anti-phospho-MYL9 (Ser19) antibody (pMLC2: 1:250, MA5-15163; Invitrogen, USA), and mouse anti-collagen type 1 antibody (Col1: 1:500, MA1-26771; Invitrogen). Subsequently, the samples were incubated with secondary antibodies, goat anti-rabbit antibody, Alexa Fluor 546 (1:500, A11010; Invitrogen) and/or goat anti-mouse antibody, Alexa Fluor 635 (1:500; A31575; Invitrogen) for 1 h at room temperature simultaneously with 4′,6-diamidino-2-phenylindole (DAPI: 1:2500, D9542; Sigma-Aldrich, USA) and Phalloidin Alexa488 (1:500, A12379; Invitrogen) for nuclear staining and filamentous actin staining, respectively.

For image acquisition, the samples were placed on chambered coverslips (80287, ibidi, Germany) and mounted in ProLong™ Gold antifade reagent (P36939; Invitrogen). Z-Stack images were acquired by a confocal microscope (TCS SP8; Leica, Germany) equipped with a $40\times$ water immersion objective lens. The images were processed and analyzed with Fiji/ImageJ.[42] All images are presented as z-stack projection images of 100 μm thickness.

2.11 | Quantification of double-strand DNA

To assess cell proliferation, double-strand DNA (dsDNA) quantification was performed using Quant-iT PicoGreen dsDNA Assay Kit (P7589; Invitrogen) according to the manufacturer's protocol. Cell lysate was obtained by repeated freeze–thaw cycle in 0.1% Triton X-100 in Milli-Q® water. The intensity of fluorescence was measured at Ex/Em = 480/520 nm using the microplate reader.

2.12 | 5-Ethynyl-2′-deoxyuridine incorporation assay

For EdU assay, 30 μM EdU was added to the growth medium on Day 3 in the static and dynamic culture. Twenty-four hours after EdU administration, the samples were fixed in ice-cold methanol for 5 min at $-20°C$. Incorporated EdU to the nuclei was detected using Click-iT™ EdU Cell Proliferation Kit for Imaging, Alexa Fluor™ 488 dye (C10337; Invitrogen) according to the manufacturer's protocol and visualized by the Leica SP8 confocal microscope.

2.13 | ALP staining

The samples collected on Day 7 were placidly fixed in 4% PFA for 2 min at room temperature. The samples were then incubated with BCIP®/NBT solusion (B5655; Sigma-Aldrich) for 30 min at room temperature. For quantification, the substrate was extracted by incubating with 100 mM cetylpyridium chloride overnight at room temperature. Absorbance was measured at 540 nm using the microplate reader.

2.14 | Alizarin Red S staining

Samples collected on Day 14 were fixed in 4% PFA for 40 min and washed gently in Milli-Q® water. Mineralized nodes were stained by 0.1% Alizarin Red S (A5533; Sigma-Aldrich) for 20 min followed by washing six times in Milli-Q® water. For quantification, the dye was extracted with 100 mM cetylpyridium chloride overnight at room temperature. Absorbance was measured at 540 nm using the microplate reader.

2.15 | Statistics

All data are represented as mean ± s.e.m unless otherwise specified. Statistical analyses were performed by using Prism 9 (Dotmatics, USA). For comparison between the static and dynamic culture conditions, Student's t-test was performed. For multiple comparisons, the data were evaluated by ANOVA followed by Dunnett's multiple comparisons test. In the cytoskeletal inhibition experiments, the mean of the chemically treated groups was compared to the control (i.e., DMSO) group only. A p value <0.05 was considered to be statistically significant.

3 | RESULTS

3.1 | CFD assessment of fluid velocity and shear stress in the bioreactor

Prior to perfusion cell culture, in silico CFD simulation was conducted to describe the distribution and magnitude of shear stress within the stack of the porous scaffolds based on micro-CT imaging of the scaffold structure (Figure 2a). A flow rate was preliminarily determined by evaluating cell growth, and 1.0 mL/min was considered optimal for the study. With the flow rate, fluid paths were evenly distributed among the stacks through the collimators, and estimated velocity field ranged from 0.1 to 0.5 mm/second (Figure 2b). Computed shear
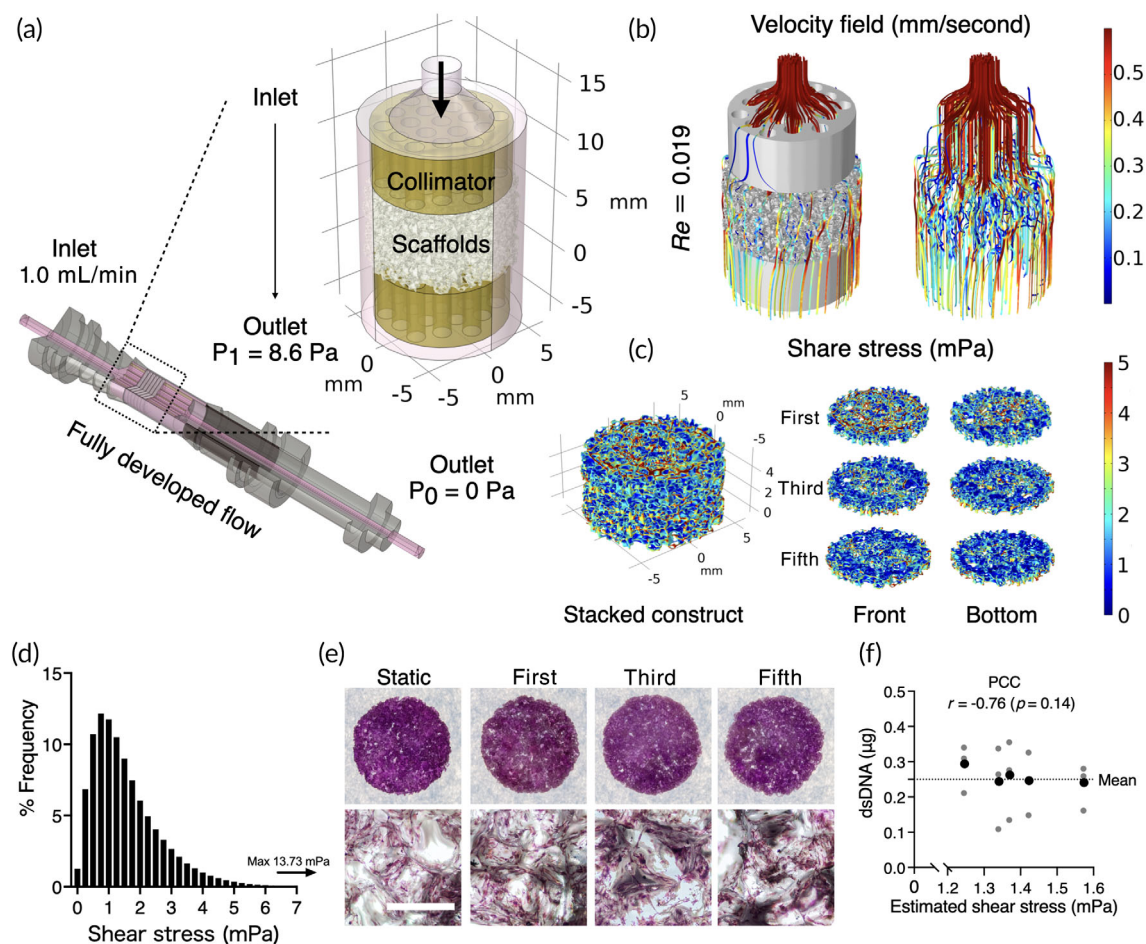
FIGURE 2 Computational fluid dynamics (CFD) for fluid shear stress estimation (a) The scaffold geometry obtained by a micro computed tomography was virtually placed in the scaffold chambers where fully developed flow at 1.0 mL/min was provided at the inlet. At the outlet of the chamber, atmospheric pressure was prescribed (P0), which determined pressure at the end of collimators on the outlet side at 8.6 Pa (P1). (b) Fluid paths were simulated evenly among the scaffolds with Reynolds number at 0.019, indicating the flow was laminar. (c) Simulation of fluid shear stress on the surfaces of first, third, and fifth scaffolds in the stack showed local shear distribution. (d) Frequent distribution of fluid shear stress ranged from 1.5e-008 to 13.73 mPa. (e) Crystal violet staining showed actual cell distribution among the scaffold stacks. (f) Pearson correlation coefficient (PCC) indicated no correlation between the estimated shear stress and harvested double-strand DNA (dsDNA) from the scaffolds at different position after 7 days of perfusion culture. Mean of harvested dsDNA (in black) were calculated from three independent samples (in gray). Scale bar = 1 mm.

stress on the surfaces showed local variation within the stack, and the highest magnitude was estimated on the surfaces the scaffold closest to the inlet (Figure 2c). Estimated shear stress ranged from 1.5e-008 to 13.73 mPa due to the heterogeneous nature of complex 3D geometry (Figure 2d). The mean and median values of estimated shear stress were 1.56 and 1.29 mPa, respectively, and over 90% of the surfaces was subjected to a range of shear stress between 0.5 and 5 mPa. DNA staining with crystal violet showed no visible difference in cell distribution between successive scaffolds in the stack (Figure 2e). Pearson correlation coefficient (PCC) did not find the correlation between the amount of dsDNA harvested and the estimated median shear stress in each scaffold, indicating that cell behaviors in the dynamic condition would be similar throughout the stack (Figure 2f).

3.2 | Fluid shear stress-induced dynamic cytoskeletal rearrangement and contractility in the 3D system

To evaluate the effect of perfusion culture on the cytoskeletal regulation, mRNA and protein expressions and enzymic activity governing cell adhesion, motility, and contractility were evaluated. Under the dynamic cell culture condition, BMSC differentially expressed genes encoding adhesion receptors (e.g., Itga2, Itga5, Itga10, and Itgb3), focal adhesion complex and actin binding proteins (e.g., Pkt2, Zyx, Pxn, Vcl, Tns2, Tns4, Vasp, and Zyx), and factors involved in Rho GTPase regulation and downstream signaling (RhoA, Rock1, Rock2, Rasgrf1, Racgap1, Rac1, Limk1, Cdc42) (Figure 3a). The gene set enrichment analysis using UniProt database identified that Ser/Thr protein kinase, cytoskeleton,
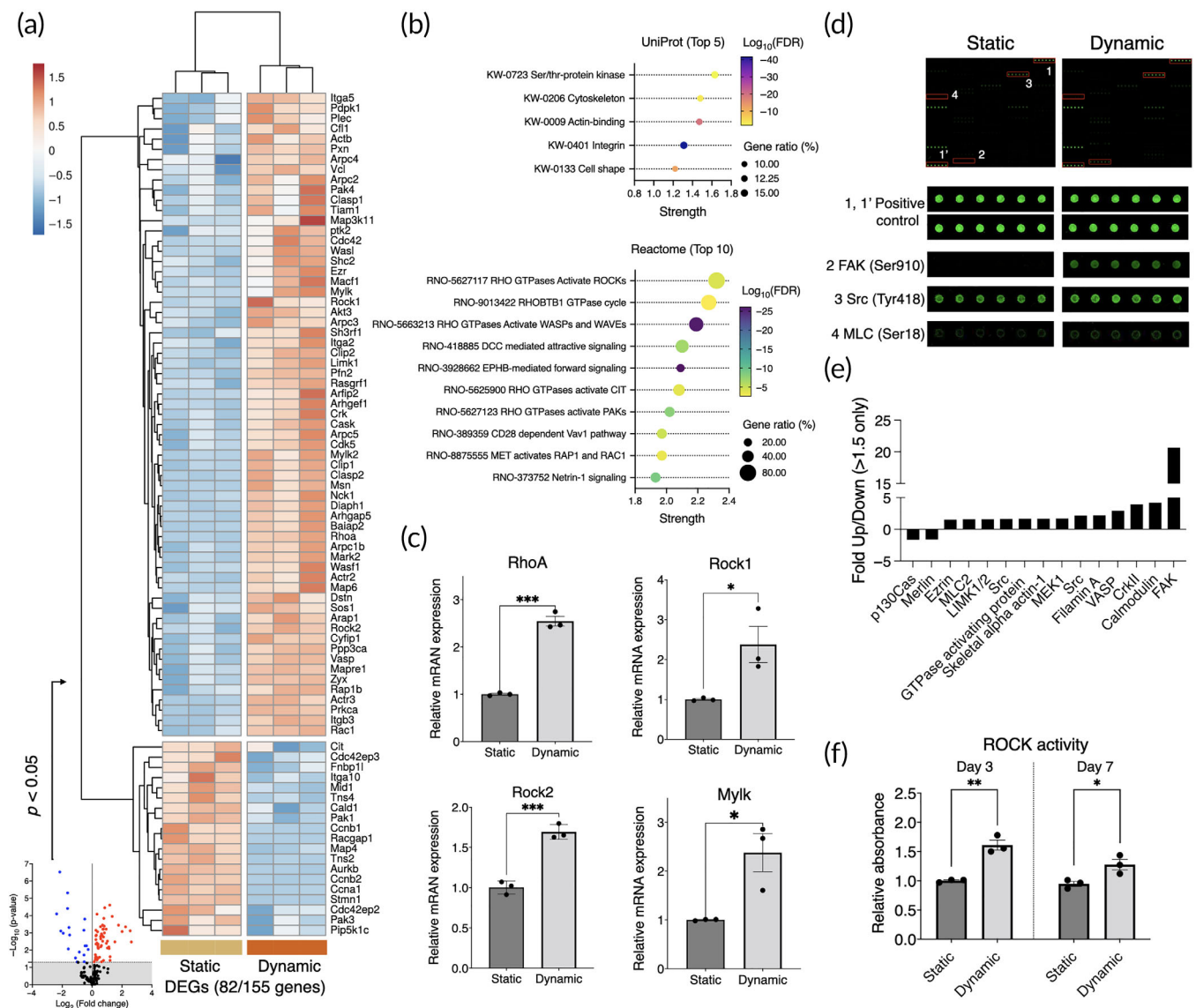
FIGURE 3 Cytoskeletal rearrangement and actomyosin contractility of BMSC in the dynamic condition. (a) Gene expression array of 155 markers encoding adhesion, migration, and cytoskeletal regulation factors. Differentially expressed genes ($p < 0.05$, DEGs) were plotted in the heatmap. Unit variance scaling was applied to $\Delta\Delta$CT values, and rows were centered. (b) Gene set enrichment analysis using UniProt and Reactome database. Top 5 enriched keywords and top 10 enriched pathways were displayed. (c) RT-qPCR analysis of Rho-ROCK signaling down to myosin light chain kinase. (d, e) Antibody microarray of cytoskeletal regulators. (f) Enzymic activity of ROCK measured by phosphorylation of myosin phosphatase target subunit 1 (MYPT1). Statistical comparison between the static and dynamic conditions was performed by Student's t-test. *$p < 0.05$; **$p < 0.01$; ***$p < 0.001$.

actin-binding, integrin, and cell shape were the highly enriched keywords. Reactome pathway analysis indicated that Rho GTPases and downstream signaling were highly enriched (Figure 3b). Validation by RT-qPCR supported the activation of Rho-ROCK signaling in the dynamic culture where RhoA ($p = 0.00012$), Rock1 ($p = 0.039$), Rock2 ($p = 0.00061$), and Mylk ($p = 0.024$) were significantly upregulated in the dynamic culture (Figure 3c). Cytoskeleton antibody microarray showed 20.7-fold increase in the expression of focal adhesion in the dynamic culture accompanied by the minor upregulation of steroid receptor coactivator (Src: 1.64-fold increase) and myosin regulatory

light chain-2 (MLC2: 1.57-fold increase) (Figure 3d,e). The enzymic activity of ROCK significantly increased after 3 days ($p = 0.002$) and 7 days ($p = 0.031$) of perfusion culture, supporting the findings from the arrays (Figure 3f).

Immunofluorescence confirmed the dynamic cytoskeletal rearrangement and contractility under perfusion culture (Figure 4a–d). BMSC under the dynamic condition showed enhanced actin polymerization, nonmuscle myosin (NM2A/2B), and phosphorylation of myosin light chain2 (MLC2), resulting in more elongated morphology compared to the static counterpart ($p = 0.0006$).
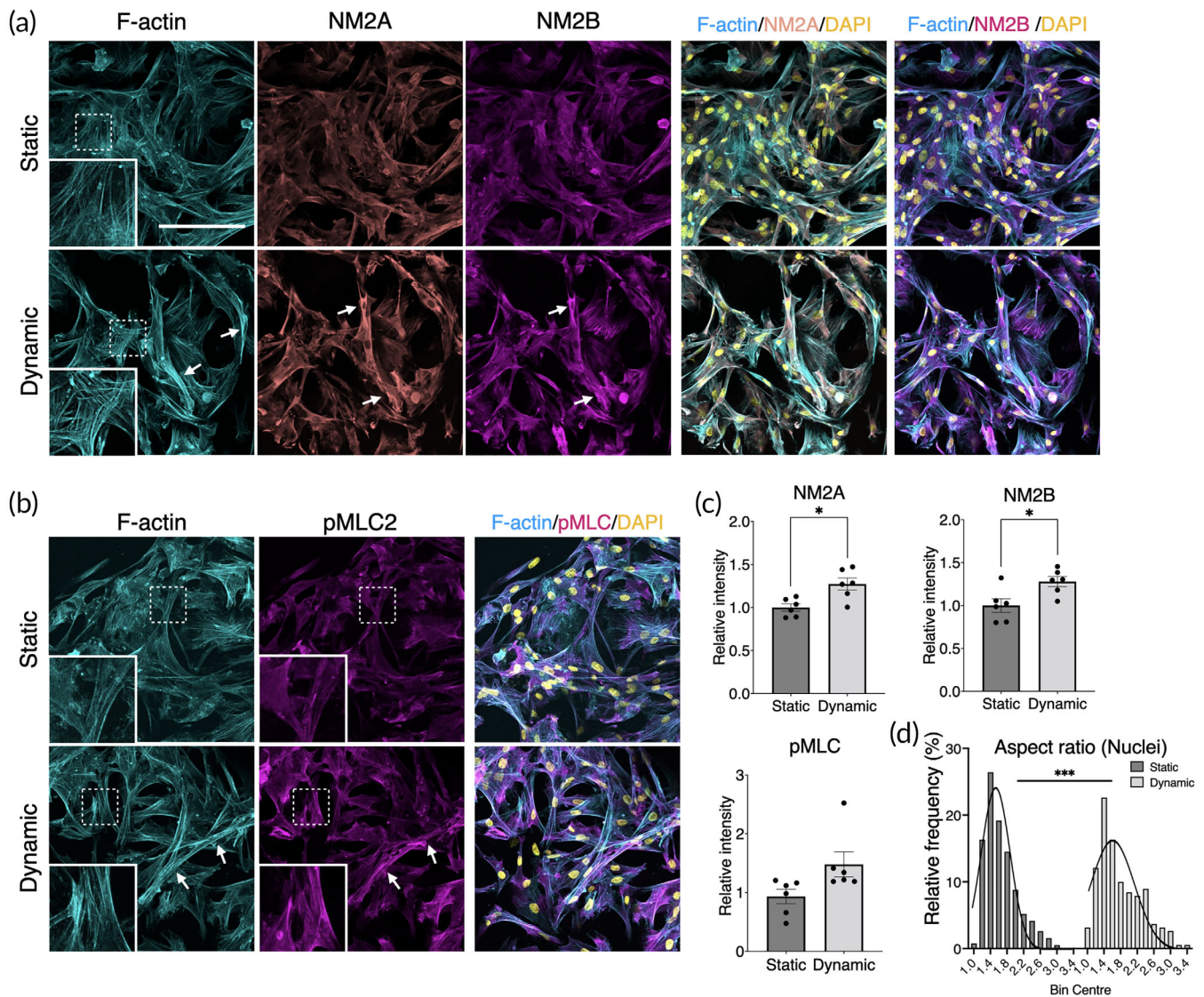
FIGURE 4 Immunofluorescence of actomyosin under static and dynamic cell culture. (a, b) In the dynamic culture condition, BMSC showed noticeable actomyosin contraction highlighted by highly polymerized filamentous actin (F-actin), nonmuscle myosin 2A (NM2A), nonmuscle myosin 2B (NM2B), and phosphorylated myosin light chain 2 (pMLC2). Arrows indicate highly contracted sites. (c) Image quantification of NM2A, NM2B, and pMLC, showing enhanced expression. (d) Cell morphometric assessment by nuclear aspect ratio supported the evidence of cell contraction ($p = 0.0006$). The fitted distribution lines were generated by Gaussian distribution equation. Statistical comparison between the static and dynamic conditions was performed by Student's t-test. $*p < 0.05$; $***p < 0.001$.

3.3 | Cell contractility is necessary for maintaining cell growth under perfusion

To evaluate the role of cell contractility in cell growth during dynamic cell culture, four different small molecule inhibitors (i.e., Rhosin, Y27632, MLCK ip 18, and Blebbistatin) were used to drive cell relaxation (Figure 5a). In the present system, we found that perfusion culture slowed cell growth (Figure 5b,c). At concentrations that did not affect dsDNA yield in the static condition, the inhibitors did prevent cells from proliferating in the dynamic cell culture (Day 3: $p = 0.0013$, Days 7–14: $p < 0.0001$). EdU incorporation assays confirmed that the reduced dsDNA yield was due to cell cycle arrest (Figure 5d,e). With

or without inhibitors, in the static condition, approximately 60% of the cells incorporated EdU in 24 hours, but only 40% did so in the dynamic condition ($p = 0.015$). Proliferation was further diminished by the inhibitors, with < 20% of the cells found to be proliferative (DMSO VS Rhosin: $p = 0.019$; Y27632: $p = 0.0098$; MLCK ip 18: $p = 0.035$; Blebbistatin: $p = 0.0046$). When actomyosin contraction was pharmacologically induced in a static culture by dosing Narciclasine or Calyculin A for 7 days, cell proliferation also significantly decreased (Figure S3A). Together, these results suggest that excess cellular contractility slows proliferation in static culture but is necessary for maintaining their proliferative status under 3D perfusion culture.
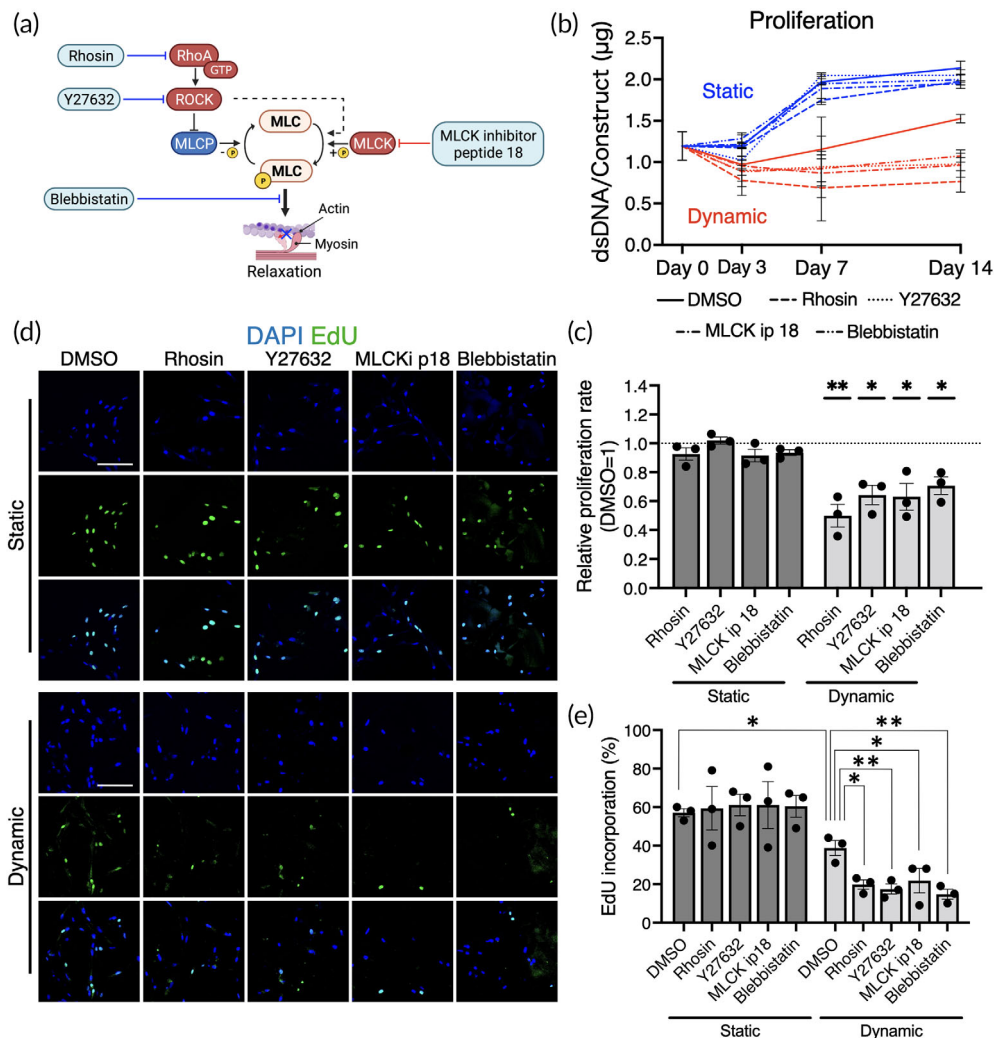
FIGURE 5 Cell growth under perfusion with/without inhibitors of actomyosin contractility. (a) Rhosin chloride (Rhosin), Y27632 dihydrochloride (Y27632), MLCK inhibitory peptide 18 (MLCK ip 18), and Blebbistatin (203390) were added to the culture medium during the dynamic cell culture, leading forcible cell relaxation. (b, c) The quantification of double strand DNA (dsDNA) demonstrated the cells in the dynamic culture were less proliferative compared to the static counterpart. The inhibition of actomyosin contractility mitigated cell proliferation in the dynamic but not static conditions. Dunnett's multiple comparison was performed by comparing to DMSO control within static and dynamic conditions. (d, e) EdU (5-ethynyl-2′-deoxyuridine) incorporation during 24 hours of cell culture, detected by confocal microscope, decreased in the dynamic condition, particularly in the presence of the inhibitors. Statistical comparison between the static and dynamic conditions without the inhibitors was performed by Student's t-test and within the groups by ANOVA followed by Dunnett's multiple comparison. $*p < 0.05$; $**p < 0.01$. Scale bar = 100 μm.

3.4 | Mechanically induced osteogenic gene expression profile differed from chemically induced osteogenesis

To elucidate the osteogenic profile of the mechanically stimulated BMSC, the expression of 84 genes associated with osteogenesis was compared between the dynamic condition, the static condition as a negative control, and the chemically osteoinductive condition (i.e., OM) as a positive control. In the dynamic condition, the BMSC upregulated 52 and 47 osteogenesis-related markers on Days 7 and 14, respectively, compared to the static counterpart (Figure 6a,b). Active metabolism of extracellular matrices during the dynamic culture featured the expression profile on Day 7 where the upregulation of mRNA encoding the major components of bone extracellular matrices such as collagen (Col1a1, Col1a2, Col2a1, Col4a1, Col7a1, and Col10a1) was observed simultaneously with the robust upregulation of matrix metalloproteinases (Mmp9, 61.62-fold, $p = 0.00010$; Mmp10, 149.66-fold, $p = 0.0069$). This trend was not observed in the OM group. The upregulated genes in the dynamic condition on Day 14 included a key transcriptional factor for osteogenesis, Runx2 (2.71-fold, $p < 0.0001$), as well as common late differentiation markers such as dentin matrix acidic phosphoprotein 1 (Dmp1, 4.38-fold, $p = 0.0012$), alkaline phosphatase (Alp, 1.21-fold, $p = 0.038$), osteopontin (Spp1, 3.28-fold, $p = 0.0025$), and bone sialoprotein
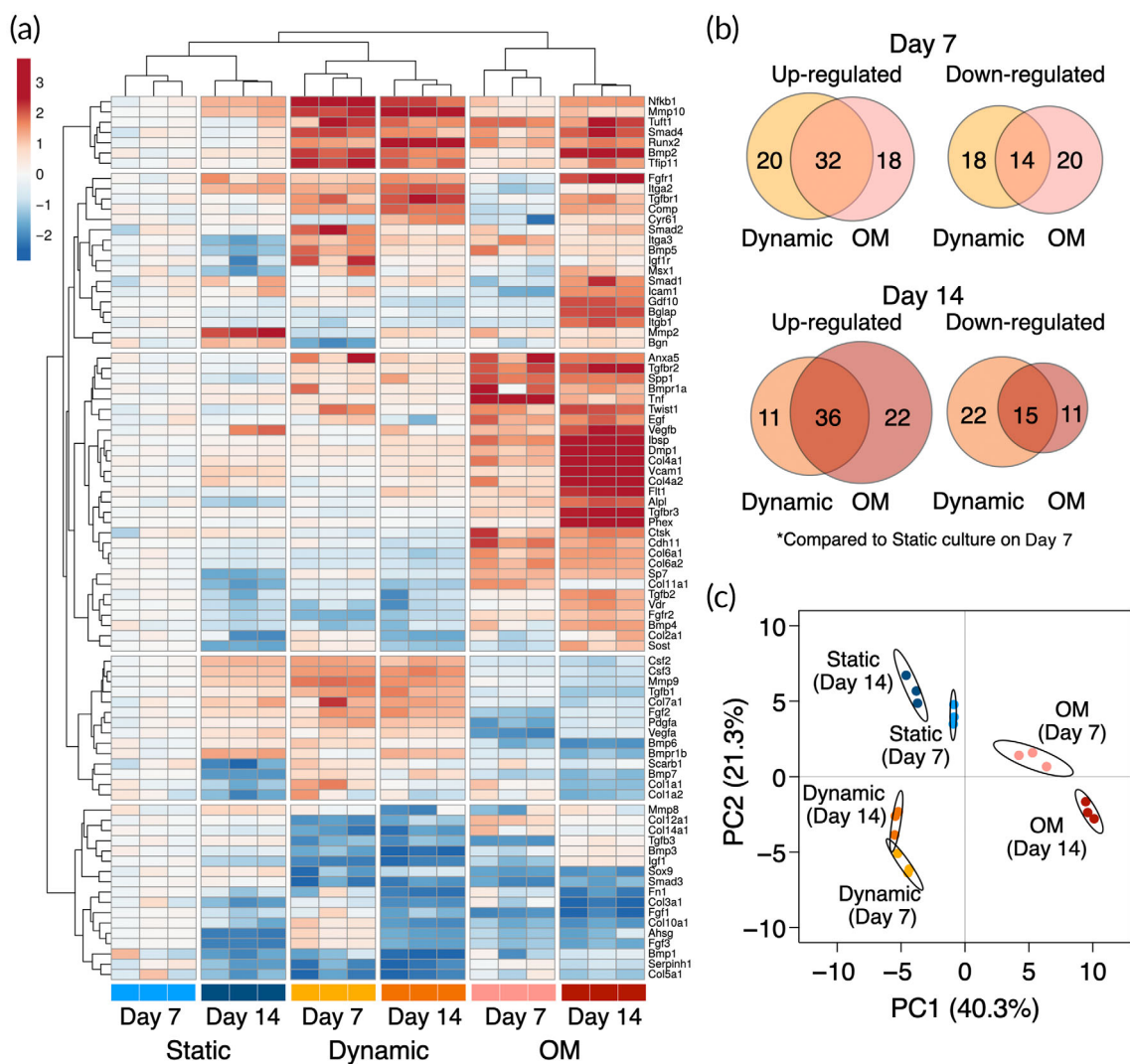
FIGURE 6 Osteogenic gene expression profile of mechanically stimulated BMSC. (a) Heatmap of mRNA expression levels showing the expression pattern of 84 osteogenesis-associated markers in the static, dynamic, and chemically stimulated conditions by osteoinductive medium (OM). Both rows and columns are clustered using Euclidean distance and complete linkage. Unit variance scaling was applied to log$_2$FC values. (b) Venn diagrams presenting number of differentially expressed gene on Days 7 and 14. (c) Principal component analysis (PCA) of osteogenic gene expression pattern. X and Y axis show principal component 1 and principal component 2 that explain 40.3% and 21.3% of the total variance, respectively. Prediction ellipses are such that with probability 0.95, a new observation from the same group will fall inside the ellipse. Samples are colored according to their conditions and timepoints.

(Ibsp, 5.15-fold, $p = 0.0021$) compared to the static counterpart. The expression of Runx2 was significantly higher in the dynamic condition than the OM group on Day 7 (1.65-fold, p-0.00077) and Day 14 (1.54-fold, $p = 0.00033$). Additionally, fibroblast growth factors (Fgfs: Fgf1, Fgf2, and Fgf3), transforming growth factor-β super-family (Tgfs: Tgfb1, Tgfb2; Bmps: Bmp2, Bmp5, Bmp6, and Bmp7) and its transducer (Smad2, Smad4), and colony-stimulating factors (Csfs: Csf2, Csf3) were found upregulated in the dynamic condition over the period. Noteworthily, a late osteogenic marker, osteocalcin (Bglap), was downregulated in both dynamic and OM groups on Day 7 compared to the static counterpart (dynamic, 0.14-fold, $p = 0.0057$; OM, 0.58-fold, $p = 0.090$). It remained downregulated in the dynamic condition (0.26-fold, $p = 0.091$) but was

significantly upregulated in the OM group (305-fold, $p < 0.0001$) on Day 14.

Despite some quantitative differences, the overall osteogenic profile in the dynamic condition remained comparable between Days 7 and 14, whereas an increase in a number of upregulated genes (50 genes on Day 7 and 58 genes on Day 14) as well as a significant increase in the quantity of the expression was observed in the OM group. This would indicate that, although perfusion culture stimulates the expression of some osteogenesis-related genes, prolonged perfusion culture may not maturate osteogenicity, at least within the 14-days period. Principal components analysis (PCA) highlighted the unique osteogenic profile of the mechanically stimulated cells with a clear separation from the static and chemically induced groups
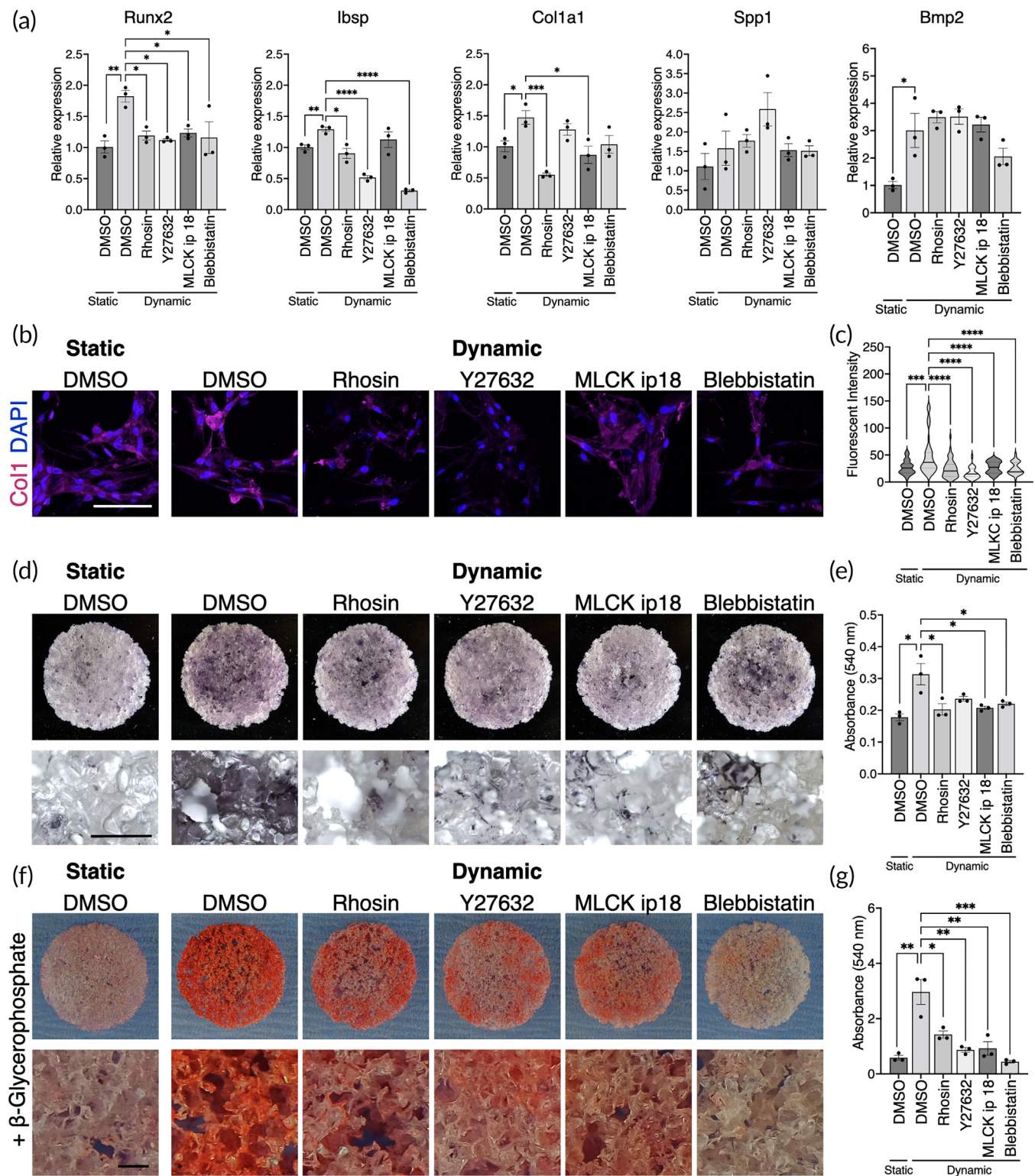
FIGURE 7 Mechanically induced osteogenesis is dependent on actomyosin contractility (a) mRNA expression levels of osteogenic markers in the static and dynamic conditions with/without the inhibitors of actomyosin contractility. (b) Immunofluorescence of type 1 collagen and (c) quantification of fluorescent intensity. (d) Alkaline phosphatase staining and (e) quantification of extracted substrate. (f) Alizarin red S staining and (g) quantification of extracted dye. The samples for the mineralization assay were cultured in the presence of β-glycerophosphate as a source of phosphate ions. Statistical comparison between the static and dynamic condition was performed by the Student's t-test and comparison among pharmacologically treated groups were by ANOVA followed by Dunnett's multiple comparison. *$p < 0.05$; **$p < 0.01$; ***$p < 0.001$; ****$p < 0.0001$. White scale bar = 100 μm, black scale bar = 500 μm.

(Figure 6c). The clusters of perfusion-induced osteogenesis were indeed shifted orthogonally to conventional osteogenic differentiation, but the subsequent experiments revealed the expression patterns still supported conventional osteogenic functionality.

3.5 | Mechanically induced osteoblastic functionality is governed by Rho-ROCK signaling and cell contractility

To investigate whether (1) the mechanically induced osteogenic profile was governed by cell contraction under perfusion and (2) the mechanically stimulated BMSC practically possessed the osteoblastic phenotype, osteogenic differentiation was further evaluated with and without the cell contraction inhibitors.

As the osteogenic profiling revealed, the expression of Runx2 (1.82-fold increase, $p = 0.0038$), Ibsp (1.29-fold increase, $p = 0.0053$), Cal1a1 (1.47-fold increase, $p = 0.030$), Spp1 (1.57-fold increase, $p = 0.45$), and Bmp2 (3.0-fold increase, $p = 0.035$) increased in the dynamic condition compared to the static counterpart on Day 7 (Figure 7a). The use of the inhibitors fully or partially counteracted the upregulation of Runx2, Ibsp, and Col1a1 but not Spp1. The mitigation of mechanically induced Bmp2 expression by the inhibitors was not statistically significant.

For the functionality assessment of the stimulated BMSC, collagen matrix formation, alkaline phosphatase activity, and calcium deposition were evaluated. While the cells in the static condition secreted type 1 collagen faintly, clusters of the cells significantly enriched collagen production in the dynamic condition (Figure 7b,c). This was depicted as an outstanding peak in the dynamic condition by the quantification ($p = 0.0002$). The inhibitors, particularly Y27632, disrupted the perfusion-enhanced collagen secretion. Similarly, ALP staining showed the upregulated ALP activity in the dynamic condition compared to the static counterpart ($p = 0.0019$), which was, however, negated by the inhibitors (Figure 7d,e). Calcium deposition was evaluated as an indicator of maturation of osteogenic differentiation by adding beta-glycerophosphate as a source of phosphate ions in the growth medium. Remarkably, the mechanically stimulated cells successfully deposited calcium nodes on the scaffolds while beta-glycerophosphate alone was not sufficient to induce mineralization in the static condition ($p = 0.0066$) (Figure 7f,g). Mineralization was attenuated by the inhibitors, particularly blebbistatin, completely masking the pro-osteogenic effect of dynamic cell culture. Taken together, dynamic cell culture in the perfusion bioreactor was sufficient to induce BMSC osteogenesis, which was dependent on enhanced cellular contractility.

4 | DISCUSSION

Using a bioreactor for 3D cell culture is a promising strategy to improve the efficiency of cell therapy in bone tissue engineering. Based on credible evidence identified in conventional monolayer cell culture studies that mechanical stimulation promotes BMSC osteogenesis, the concept has been brought to 3D systems for translational research. However, due to the complexity of 3D cell culture in a dynamic environment, the knowledge gained so far seems fragmented, particularly when in the absence of osteoinductive medium. This is because in different bioreactor systems developed for bone tissue engineering not only dynamic conditions but also basic cell culture factors such as volume of medium, humidification method, and static pressure may differ.[39,43,44] The chemical and physical properties of scaffolding materials may also synergistically influence cellular behaviors in a dynamic environment. Additionally, the precise evaluation of fluid dynamics with 3D scaffolds requires high computational cost, which may not always be affordable.[45] Consequently, flow is often described only by flow rate (e.g., mL/min) or pump speed (e.g., rpm), but not the magnitude of fluid force exerted on cells.[46] These factors make it difficult to interpret experimental findings from different models. In the present study by culturing BMSC in the perfusion bioreactor, the comprehensive analyses of cell behaviors under perfusion culture were performed including detailed CFD analysis, cell morphological assessment, cell growth, and mechanically induced osteogenesis in the absence of osteoinductive medium.

In the present study, the optimal flow rate was preliminarily determined as 1.0 mL/min in the system. The flow rate corresponded to estimated shear stress of approximately 0.5–5 mPa (mean 1.56 mPa) to which most of BMSC on the scaffolds were exposed. Fluid paths were estimated to be distributed uniformity throughout the constructs, which is an important aspect of the dynamic culture to improve mass transfer from/to the constructs although a magnitude of fluid shear varied spatially. BMSC and osteoblastic cells are reportedly more vulnerable to fluidic stimulation on 3D porous scaffolds compared to the 2D monolayered counterpart, and excessive shear stress can lead to apoptosis.[21,37,47–52] This could be because cell morphological adaptation and migration are restricted to the geometry of scaffolds when fluid stimuli act in multiple directions.[53] It was therefore no surprise that the shear stress used in our study, although considerably lower than that reported to promote osteogenesis in the conventional 2D systems, was sufficient to provoke dynamic cellular behaviors.

Under this level of perfusion, BMSC clearly showed a sign of morphological change with a number of upregulated factors for cell morphogenesis including surface mechanoreceptors, focal adhesion complex, and the direct inducers of actomyosin contractility. Elevated actomyosin contractility directly links to BMSC fate determination as a process and an endpoint. The angular, elongated morphology and increased rheological stiffness of BMSC is associated with high expression of actomyosin and focal adhesion and with osteoblast fate, whereas rounded morphology, low cell stiffness and lower actomyosin and focal adhesion expression is associated with adipogenic differentiation.[54–56] Therefore, it would be reasonable to mention that the cytoskeletal features exhibited by the BMSC in the present system favored osteogenic differentiation.

Our results indicated that perfusion culture delayed cell proliferation, possibly mediated by cell contraction. The reported effect of

perfusion culture on cell proliferation is inconsistent in the published literature in both 2D and 3D systems. There are studies reporting mitogenic effects,[11,12,30,33,57–60] anti-mitogenic effects,[15,16,32,36,61] and no effect,[14,34] while all promoting osteogenic phenotypes. The inconsistency could arise from differences in the magnitude of shear stress, the type of cells used, measurement methodology, and/or the efficiency of passive nutrient transport within scaffolding material since low-diffusive scaffolds would benefit from perfusion more than highly permeable materials with the respect to nutrient transport. Previous studies in a 2D cell culture model demonstrated that laminar shear stress reduces MSC proliferation in a dose-dependent manner by arresting cell cycle at G_0/G_1 phases.[51,62] In the present study, where the highly porous scaffolds with macropores were used, the reduction of cell proliferation could be attributed largely to shear stress on the cells. The cell contractility inhibitors of Rho, ROCK, MLCK, and myosin II blocked cell cycle further and hindered cell proliferation in the dynamic condition. Taken together, increased cell contraction caused by shear stress was associated with reduced cell proliferation, but contractility was indeed necessary for maintaining proliferation under flow.

Mechanically induced or promoted osteogenic differentiation is often measured by increased ALP activity and the upregulation of key osteogenic markers, such as Runx2. However, the term "osteogenic differentiation" has been used casually without sufficient definition, and the overall osteogenic profile under mechanical stimulation has not hitherto been adequately described. The present study highlighted the unique osteogenic profile of BMSC stimulated by fluid flow. Even in the absence of the osteoinductive supplements, fluid shear stress stimulated the mRNA expression of osteogenic markers, such as Runx2, Alp, and Ibsp. Interestingly, the expression of Runx2 was significantly higher in the dynamic condition than the OM group, and signaling molecules such as Bmps, Fgfs, Csfs, and Tgfs were differentially expressed. This has revealed that fluid shear stress may induce osteogenic differentiation differently from the conventionally described differentiation by the OM. Nevertheless, the functionality gained by the mechanically stimulated BMSC reconciled with typical preosteoblast-like phenotypes, featured by an increase in type 1 collagen formation and ALP activity. It is generally considered that, in the absence of the osteoinductive supplements, mechanical stimulation promotes ALP activity and the expression of early osteogenic markers, but it is not sufficient to induce osteoblastic maturation characterized by the upregulation of Bglap and mineralization.[21,23,24,57–59] Here, by adding beta-glycerophosphate as a source of inorganic phosphate ions in the growth medium, we demonstrated that the mechanically stimulated BMSC were capable of depositing calcium nodes despite a lack of Bglap expression. In fact, the initiation of mineralization precedes the significant upregulation of Bglap in vitro,[38] suggesting that the mechanically stimulated BMSC indeed possessed the phenotype of moderately mature osteoblastic cells. The inhibition of actomyosin contractility under flow significantly mitigated their osteogenic functionality, confirming that cytoskeletal rearrangement via Rho-ROCK signaling is necessary for the osteogenic responses triggered by fluidic stimuli in the absence of osteoinductive medium. Nevertheless, the

mechanically upregulated osteogenic markers were not consistently suppressed by the inhibitors. Previous studies have shown that fluid shear stress at physiological levels modulates various pathways such as ERK/MAPK signaling, P38 signaling, TGFβ signaling, Hedgehog signaling, Notch signaling, and Wnt signaling pathways in MSC as well as osteoblasts and osteocytes.[16,21,63–65] The regulation of osteogenic genes is multifactorial, and these pathway may interplay with osteogenic genes differently, which may bypass the Rho-ROCK-mediated cell contraction. Although this study does not enter the debate as to whether Rho-ROCK activation and/or cell contraction are sufficient to induce osteogenesis, we observed that the pharmacological activation of Rho by Narciclasine significantly modulated the mRNA expression level of Runx2 and Bmp2 (Figure S3B). The upregulation of Bmp2 was also induced by the inhibition of myosin phosphatase, Calyculin A. However, both drugs significantly decreased Col1a1 expression, and we did not find a rational correlation between cell contractility and ALP activity from the preliminary data (Figure S3C,D). It would be therefore reasonable to conclude that osteogenic induction by fluid stimuli is governed by, but not limited to, Rho-ROCK-mediated cytoskeletal modulation.

Translation of knowledge in mechanobiology into the field of tissue engineering has successfully paved the way for the development of prominent dynamic cell culture platforms for regenerative medicine. This will facilitate effective 3D cell culture and improve cell-based therapy for bone regeneration. To bring mechanically stimulated cells into clinical settings, it is necessary to accurately grasp cell response to dynamic environment for safety and efficacy. Each system is unique, and bioreactor designs, material selection, scaffold geometry, supplemented drugs, cell origin, and other environmental factors synergistically or reciprocally interact with resulting cell behaviors.[66,67] More to the point, biological variables attributable to donors such as age, gender, systemic conditions, and epigenetics need to be taken into consideration when it comes to clinical application.[68] In the study, male Lewis rats were used as a source of BMSC because of the abundancy of BMSC compared to female animals.[69] Admittedly, our observation needs to be verified by human cells isolated from donors with various background. Therefore, further in-depth studies using diverse experimental settings are required to fully elucidate mechanically induced osteogenesis and its potential for future clinical translation.

AUTHOR CONTRIBUTIONS

(equal); project administration (equal); resources (equal); software (equal); supervision (equal); validation (equal); writing – original draft (supporting); writing – review and editing (equal). **Jeremy Green:** Conceptualization (equal); formal analysis (equal); methodology (equal); writing – original draft (equal); writing – review and editing (equal). **Thomas Schwarz:** Methodology (equal); resources (equal); writing – original draft (equal); writing – review and editing (equal). **Kamal Mustafa:** Conceptualization (equal); formal analysis (equal); funding acquisition (lead); investigation (equal); methodology (equal); project administration (lead); resources (equal); supervision (lead); validation (equal); writing – original draft (equal); writing – review and editing (equal).

CONFLICT OF INTEREST STATEMENT

The authors declare no potential conflicts of interest with respect to the authorship and/or publication of this article.

PEER REVIEW

The peer review history for this article is available at https://www.webofscience.com/api/gateway/wos/peer-review/10.1002/btm2.10509.

DATA AVAILABILITY STATEMENT

The raw data supporting the conclusion of this article will be made available by the authors, without undue reservation.

ORCID

Shuntaro Yamada https://orcid.org/0000-0003-0282-5498

REFERENCES

1. Lane SW, Williams DA, Watt FM. Modulating the stem cell niche for tissue regeneration. *Nat Biotechnol*. 2014;32:795-803.
2. Maul TM, Chew DW, Nieponice A, Vorp DA. Mechanical stimuli differentially control stem cell behavior: morphology, proliferation, and differentiation. *Biomech Model Mechanobiol*. 2011;10:939-953.
3. Gurkan UA, Akkus O. The mechanical environment of bone marrow: a review. *Ann Biomed Eng*. 2008;36:1978-1991.
4. Castillo AB, Jacobs CR. Mesenchymal stem cell mechanobiology. *Curr Osteoporos Rep*. 2010;8:98-104.
5. Metzger TA, Schwaner SA, LaNeve AJ, Kreipke TC, Niebur GL. Pressure and shear stress in trabecular bone marrow during whole bone loading. *J Biomech*. 2015;48:3035-3043.
6. Sun Y, Yuan Y, Wu W, Lei L, Zhang L. The effects of locomotion on bone marrow mesenchymal stem cell fate: insight into mechanical regulation and bone formation. *Cell Biosci*. 2021;11:88.
7. Zhong Z, Akkus O. Effects of age and shear rate on the rheological properties of human yellow bone marrow. *Biorheology*. 2011;48:89-97.
8. Bethel M, Chitteti BR, Srour EF, Kacena MA. The changing balance between osteoblastogenesis and adipogenesis in aging and its impact on hematopoiesis. *Curr Osteoporos Rep*. 2013;11:99-106.
9. Justesen J, Stenderup K, Ebbesen EN, Mosekilde L, Steiniche T, Kassem M. Adipocyte tissue volume in bone marrow is increased with aging and in patients with osteoporosis. *Biogerontology*. 2001;2:165-171.
10. Gao X, Zhang X, Xu H, Zhou B, Wen W, Qin J. Regulation of cell migration and osteogenic differentiation in mesenchymal stem cells under extremely low fluidic shear stress. *Biomicrofluidics*. 2014;8:052008.
11. Elashry MI, Gegnaw ST, Klymiuk MC, Wenisch S, Arnhold S. Influence of mechanical fluid shear stress on the osteogenic differentiation protocols for equine adipose tissue-derived mesenchymal stem cells. *Acta Histochem*. 2019;121:344-353.
12. Kapur S, Baylink DJ, William Lau K-H. Fluid flow shear stress stimulates human osteoblast proliferation and differentiation through multiple interacting and competing signal transduction pathways. *Bone*. 2003;32:241-251.
13. Liu L, Shao L, Li B, et al. Extracellular signal-regulated kinase1/2 activated by fluid shear stress promotes osteogenic differentiation of human bone marrow-derived mesenchymal stem cells through novel signaling pathways. *Int J Biochem Cell Biol*. 2011;43:1591-1601.
14. Kreke MR, Goldstein AS. Hydrodynamic shear stimulates osteocalcin expression but not proliferation of bone marrow stromal cells. *Tissue Eng*. 2004;10:780-788.
15. Kreke M, Huckle W, Goldstein A. Fluid flow stimulates expression of osteopontin and bone sialoprotein by bone marrow stromal cells in a temporally dependent manner. *Bone*. 2005;36:1047-1055.
16. Zhao Y, Richardson K, Yang R, et al. Notch signaling and fluid shear stress in regulating osteogenic differentiation. *Front Bioeng Biotechnol*. 2022;10:1-14.
17. Kim KM, Choi YJ, Hwang J-H, et al. Shear stress induced by an interstitial level of slow flow increases the osteogenic differentiation of mesenchymal stem cells through TAZ activation. *PLoS One*. 2014;9:e92427.
18. Dash SK, Sharma V, Verma RS, Das SK. Low intermittent flow promotes rat mesenchymal stem cell differentiation in logarithmic fluid shear device. *Biomicrofluidics*. 2020;14:054107.
19. Pasini A, Lovecchio J, Ferretti G, Giordano E. Medium perfusion flow improves osteogenic commitment of human stromal cells. *Stem Cells Int*. 2019;2019:1-10.
20. Sonam S, Sathe SR, Yim EKF, Sheetz MP, Lim CT. Cell contractility arising from topography and shear flow determines human mesenchymal stem cell fate. *Sci Rep*. 2016;6:20415.
21. Yourek G, McCormick SM, Mao JJ, Reilly GC. Shear stress induces osteogenic differentiation of human mesenchymal stem cells. *Regen Med*. 2010;5:713-724.
22. Li Y, Wang J, Zhong W. Regulation and mechanism of YAP/TAZ in the mechanical microenvironment of stem cells (review). *Mol Med Rep*. 2021;24:506.
23. Hu K, Sun H, Gui B, Sui C. TRPV4 functions in flow shear stress induced early osteogenic differentiation of human bone marrow mesenchymal stem cells. *Biomed Pharmacother*. 2017;91:841-848.
24. Jiao F, Xu J, Zhao Y, et al. Synergistic effects of fluid shear stress and adhesion morphology on the apoptosis and osteogenesis of mesenchymal stem cells. *J Biomed Mater Res Part A*. 2022;110:1636-1644.
25. Bergemann C, Elter P, Lange R, et al. Cellular nutrition in complex three-dimensional scaffolds: a comparison between experiments and computer simulations. *Int J Biomater*. 2015;2015:1-12.
26. Rouwkema J, Koopman BFJM, Van Blitterswijk CA, Dhert WJA, Malda J. Supply of nutrients to cells in engineered tissues. *Biotechnol Genet Eng Rev*. 2009;26:163-178.
27. Martin I, Smith T, Wendt D. Bioreactor-based roadmap for the translation of tissue engineering strategies into clinical products. *Trends Biotechnol*. 2009;27:495-502.
28. Moser C, Bardsley K, El Haj AJ, Alini M, Stoddart MJ, Bara JJ. A perfusion culture system for assessing bone marrow stromal cell differentiation on PLGA scaffolds for bone repair. *Front Bioeng Biotechnol*. 2018;6:161.

29. Harvestine JN, Gonzalez-Fernandez T, Sebastian A, et al. Osteogenic preconditioning in perfusion bioreactors improves vascularization and bone formation by human bone marrow aspirates. *Sci Adv*. 2020;6: eaay2387.

30. Birru B, Mekala NK, Parcha SR. Improved osteogenic differentiation of umbilical cord blood MSCs using custom made perfusion bioreactor. *Biom J*. 2018;41:290-297.

31. Kleinhans C, Mohan RR, Vacun G, et al. A perfusion bioreactor system efficiently generates cell-loaded bone substitute materials for addressing critical size bone defects. *Biotechnol J*. 2015;10:1727-1738.

32. Egger D, Spitz S, Fischer M, et al. Application of a parallelizable perfusion bioreactor for physiologic 3D cell culture. *Cells Tissues Organs*. 2017;203:316-326.

33. Shi F, Xiao D, Zhang C, Zhi W, Liu Y, Weng J. The effect of macropore size of hydroxyapatite scaffold on the osteogenic differentiation of bone mesenchymal stem cells under perfusion culture., Regen. *Biomaterials*. 2021;8:rbab050.

34. Gomes ME, Sikavitsas VI, Behravesh E, Reis RL, Mikos AG. Effect of flow perfusion on the osteogenic differentiation of bone marrow stromal cells cultured on starch-based three-dimensional scaffolds. *J Biomed Mater Res*. 2003;67A:87-95.

35. Pereira AR, Lipphaus A, Ergin M, et al. Modeling of the human bone environment: mechanical stimuli guide mesenchymal stem cell–extracellular matrix interactions. *Materials (Basel)*. 2021;14:4431.

36. Yamada S, Yassin MA, Schwarz T, Hansmann J, Mustafa K. Induction of osteogenic differentiation of bone marrow stromal cells on 3D polyester-based scaffolds solely by subphysiological fluidic stimulation in a laminar flow bioreactor. *J Tissue Eng*. 2021;12: 20417314211019376.

37. Gaspar DA, Gomide V, Monteiro FJ. The role of perfusion bioreactors in bone tissue engineering. *Biomatter*. 2012;2:167-175.

38. Yamada S, Yassin MA, Weigel T, Schmitz T, Hansmann J, Mustafa K. Surface activation with oxygen plasma promotes osteogenesis with enhanced extracellular matrix formation in three-dimensional microporous scaffolds. *J Biomed Mater Res A*. 2021;109:1560-1574.

39. Yamada S, Yassin MA, Schwarz T, Mustafa K, Hansmann J. Optimization and validation of a custom-designed perfusion bioreactor for bone tissue engineering: flow assessment and optimal culture environmental conditions. *Front Bioeng Biotechnol*. 2022;10:811942.

40. Zhao F, Melke J, Ito K, van Rietbergen B, Hofmann S. A multiscale computational fluid dynamics approach to simulate the micro-fluidic environment within a tissue engineering scaffold with highly irregular pore geometry. *Biomech Model Mechanobiol*. 2019;18:1965-1977.

41. Livak KJ, Schmittgen TD. Analysis of relative gene expression data using real-time quantitative PCR and the 2(-Delta Delta C(T)) method. *Methods*. 2001;25:402-408.

42. Schindelin J, Arganda-Carreras I, Frise E, et al. An open source platform for biological image analysis. *Nat Methods*. 2012;9:676-682.

43. Schuerlein S, Schwarz T, Krziminski S, et al. A versatile modular bioreactor platform for tissue engineering. *Biotechnol J*. 2017;12:1600326.

44. Schreivogel S, Kuchibhotla V, Knaus P, Duda GN, Petersen A. Load-induced osteogenic differentiation of mesenchymal stromal cells is caused by mechano-regulated autocrine signaling. *J Tissue Eng Regen Med*. 2019;13:1992-2008.

45. Maes F, Claessens T, Moesen M, Van Oosterwyck H, Van Ransbeeck P, Verdonck P. Computational models for wall shear stress estimation in scaffolds: a comparative study of two complete geometries. *J Biomech*. 2012;45:1586-1592.

46. Sladkova M, de Peppo G. Bioreactor systems for human bone tissue engineering. *Processes*. 2014;2:494-525.

47. McAllister TN, Du T, Frangos JA. Fluid shear stress stimulates prostaglandin and nitric oxide release in bone marrow-derived preosteoclast-like cells. *Biochem Biophys Res Commun*. 2000;270: 643-648.

48. Jiang G-L, White CR, Stevens HY, Frangos JA. Temporal gradients in shear stimulate osteoblastic proliferation via ERK1/2 and retinoblastoma protein. *Am J Physiol Metab*. 2002;283:E383-E389.

49. Lim KT, Hexiu J, Kim J, Seonwoo H, Choung P-H, Chung JH. Synergistic effects of orbital shear stress on In vitro growth and osteogenic differentiation of human alveolar bone-derived mesenchymal stem cells. *Biomed Res Int*. 2014;2014:1-18.

50. Liu Y-S, Liu Y-A, Huang C-J, et al. Mechanosensitive TRPM7 mediates shear stress and modulates osteogenic differentiation of mesenchymal stromal cells through Osterix pathway. *Sci Rep*. 2015;5:16522.

51. Yu L, Ma X, Sun J, et al. Fluid shear stress induces osteoblast differentiation and arrests the cell cycle at the G0 phase via the ERK1/2 pathway. *Mol Med Rep*. 2017;16:8699-8708.

52. Porter B, Zauel R, Stockman H, Guldberg R, Fyhrie D. 3-D computational modeling of media flow through scaffolds in a perfusion bioreactor. *J Biomech*. 2005;38:543-549.

53. Zhao F, Xiong Y, Ito K, van Rietbergen B, Hofmann S. Porous geometry guided micro-mechanical environment within scaffolds for cell mechanobiology study in bone tissue engineering. *Front Bioeng Biotechnol*. 2021;9:736489.

54. Kilian KA, Bugarija B, Lahn BT, Mrksich M. Geometric cues for directing the differentiation of mesenchymal stem cells. *Proc Natl Acad Sci*. 2010;107:4872-4877.

55. Schillers H, Wälte M, Urbanova K, Oberleithner H. Real-time monitoring of cell elasticity reveals oscillating myosin activity. *Biophys J*. 2010;99:3639-3646.

56. Mathieu PS, Loboa EG. Cytoskeletal and focal adhesion influences on mesenchymal stem cell shape, mechanical properties, and differentiation down osteogenic, adipogenic, and chondrogenic pathways. *Tissue Eng Part B Rev*. 2012;18:436-444.

57. Bjerre L, Bünger CE, Kassem M, Mygind T. Flow perfusion culture of human mesenchymal stem cells on silicate-substituted tricalcium phosphate scaffolds. *Biomaterials*. 2008;29:2616-2627.

58. Sailon AM, Allori AC, Davidson EH, Reformat DD, Allen RJ, Warren SM. A novel flow-perfusion bioreactor supports 3D dynamic cell culture. *J Biomed Biotechnol*. 2009;2009:1-7.

59. Lembong J, Lerman MJ, Kingsbury TJ, Civin CI, Fisher JP. A fluidic culture platform for spatially patterned cell growth, differentiation, and cocultures. *Tissue Eng Part A*. 2018;24:1715-1732.

60. Bancroft GN, Sikavitsas VI, van den Dolder J, et al. Fluid flow increases mineralized matrix deposition in 3D perfusion culture of marrow stromal osteoblasts in a dose-dependent manner. *Proc Natl Acad Sci*. 2002;99:12600-12605.

61. Cartmell SH, Porter BD, García AJ, Guldberg RE. Effects of medium perfusion rate on cell-seeded three-dimensional bone constructs in vitro. *Tissue Eng*. 2003;9:1197-1203.

62. Luo W, Xiong W, Zhou J, et al. Laminar shear stress delivers cell cycle arrest and anti-apoptosis to mesenchymal stem cells. *Acta Biochim Biophys Sin (Shanghai)*. 2011;43:210-216.

63. Monteiro DA, Dole NS, Campos JL, et al. Fluid shear stress generates a unique signaling response by activating multiple TGFβ family type I receptors in osteocytes. *FASEB J*. 2021;35:e21263.

64. Lau K-HW, Kapur S, Kesavan C, Baylink DJ. Up-regulation of the Wnt, estrogen receptor, insulin-like growth factor-I, and bone morphogenetic protein pathways in C57BL/6J osteoblasts as opposed to C3H/HeJ osteoblasts in part contributes to the differential anabolic response to fluid shear. *J Biol Chem*. 2006;281: 9576-9588.

65. Johnson GP, Fair S, Hoey DA. Primary cilium-mediated MSC mechanotransduction is dependent on Gpr161 regulation of hedgehog signalling. *Bone*. 2021;145:115846.

66. Osborne JM, O'Dea RD, Whiteley JP, Byrne HM, Waters SL. The influence of bioreactor geometry and the mechanical environment on engineered tissues. *J Biomech Eng*. 2010;132:051006.

67. Ahmed S, Chauhan VM, Ghaemmaghami AM, Aylott JW. New generation of bioreactors that advance extracellular matrix modelling and tissue engineering. *Biotechnol Lett*. 2019;41:1-25.

68. Siddappa R, Licht R, van Blitterswijk C, de Boer J. Donor variation and loss of multipotency during in vitro expansion of human mesenchymal stem cells for bone tissue engineering. *J Orthop Res*. 2007;25:1029-1041.

69. Strube P, Mehta M, Baerenwaldt A, et al. Sex-specific compromised bone healing in female rats might be associated with a decrease in mesenchymal stem cell quantity. *Bone*. 2009;45:1065-1072.

SUPPORTING INFORMATION

Additional supporting information can be found online in the Supporting Information section at the end of this article.

How to cite this article: Yamada S, Yassin MA, Torelli F, et al. Unique osteogenic profile of bone marrow stem cells stimulated in perfusion bioreactor is Rho-ROCK-mediated contractility dependent. *Bioeng Transl Med*. 2023;e10509. doi:10.1002/btm2.10509
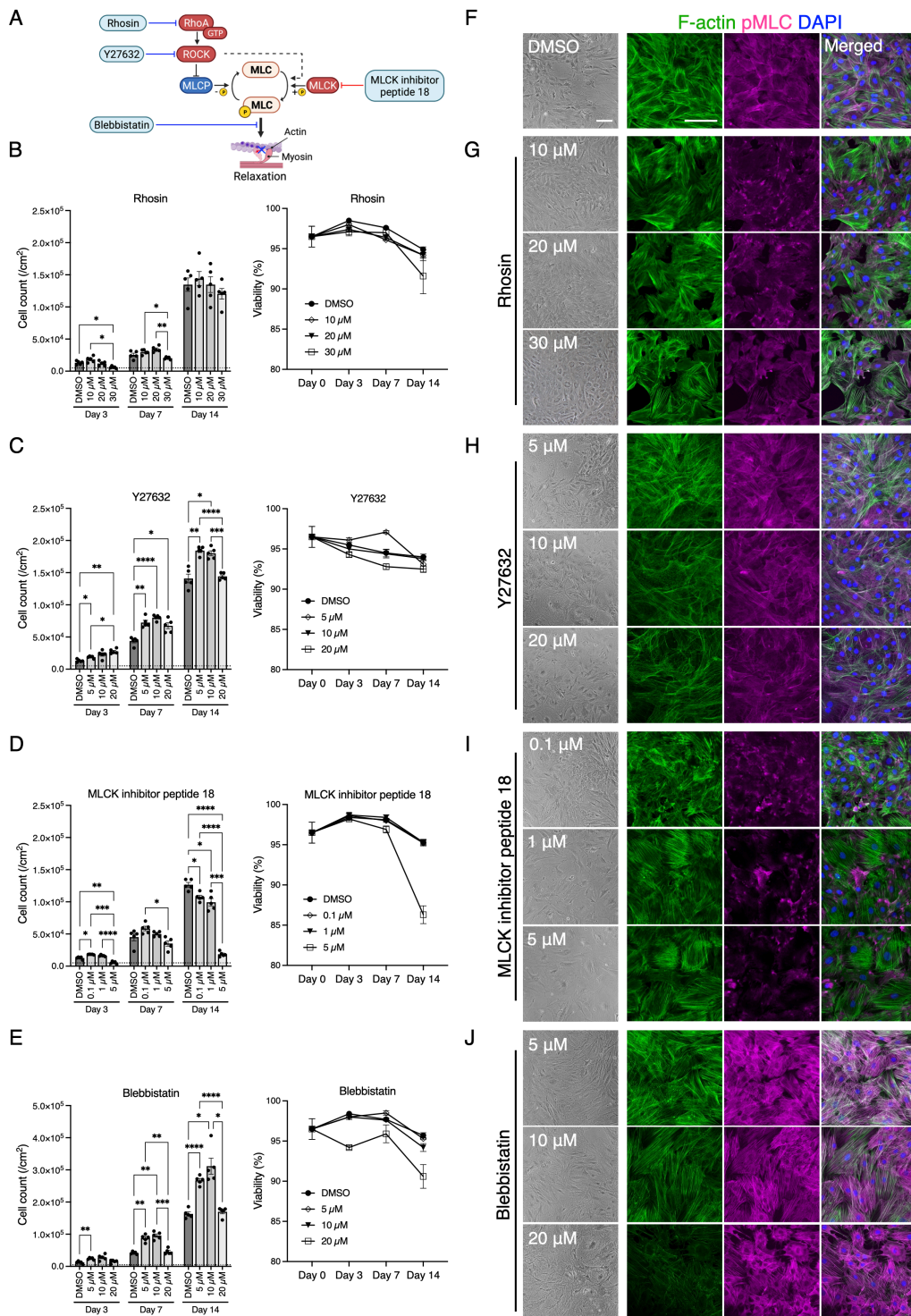
Fig. S1 Optimization of inhibitors for suppressing actomyosin contractility

(A) Rhosin chloride (Rhosin), Y27632 dihydrochloride (Y27632), MLCK inhibitory peptide 18 (MLCK ip 18), and Blebbistatin (203390) were applied to inhibit Rho, ROCK, myosin light chain kinase (MLCK), and myosin II, respectively to forcibly trigger cell relaxation. (B-J) Cell growth, viability, and actomyosin contraction were evaluated to optimize the working concentrations. * $p<0.05$, ** $p<0.01$, *** $p<0.001$, **** $p<0.0001$. Scale bar = 100 μm.
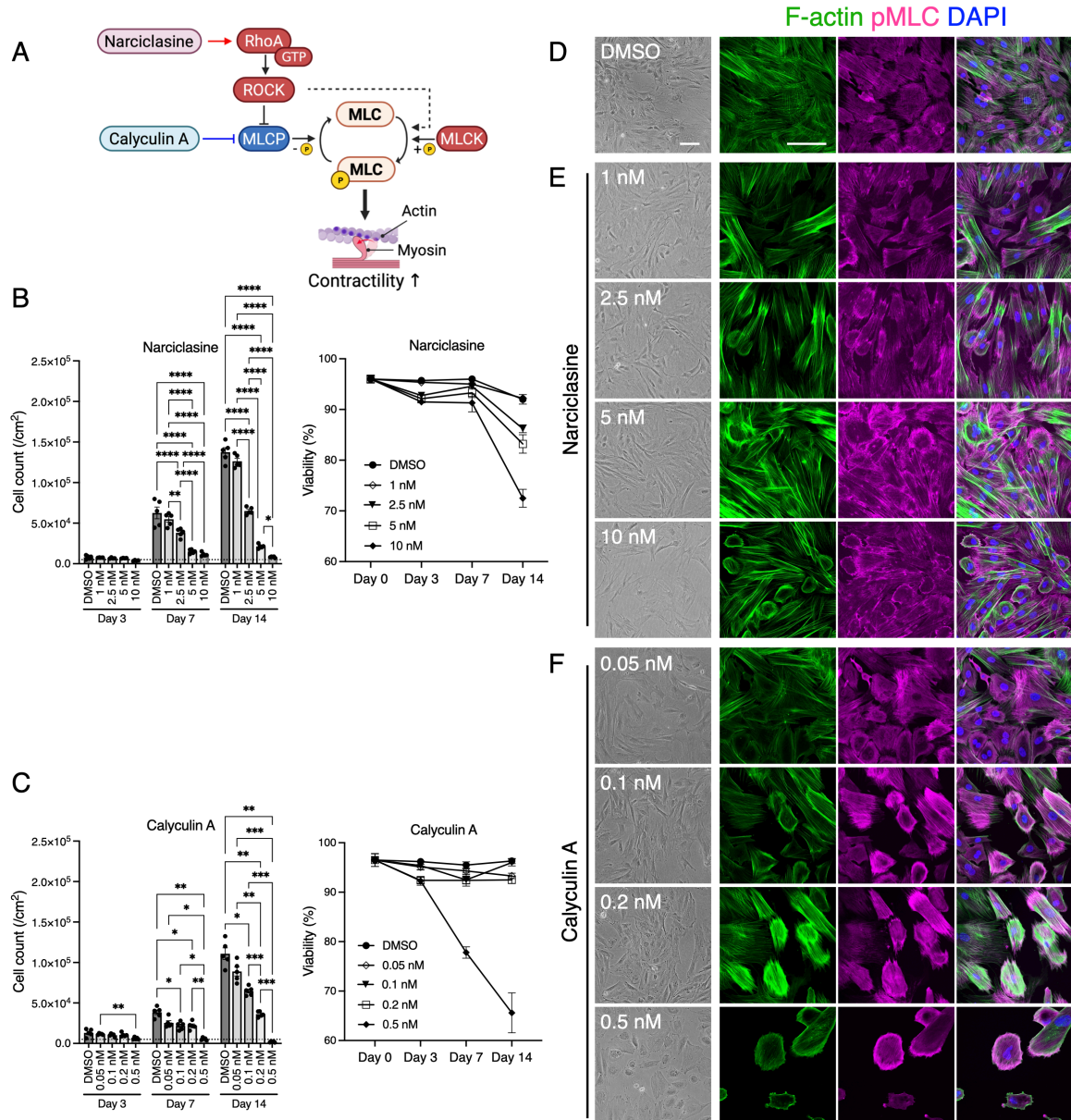
Fig. S2 Optimization of enhancers of actomyosin contractility

(A) Narciclasine and Calyculin A were applied to activate Rho and to inhibit myosin light chain phosphatase (MLCP) to forcibly trigger cell contraction. (B-F) Cell growth, viability, and actomyosin contraction were evaluated to optimize the working concentrations. * p<0.05, ** p<0.01, *** p<0.001, **** p<0.0001. Scale bar = 100 μm.
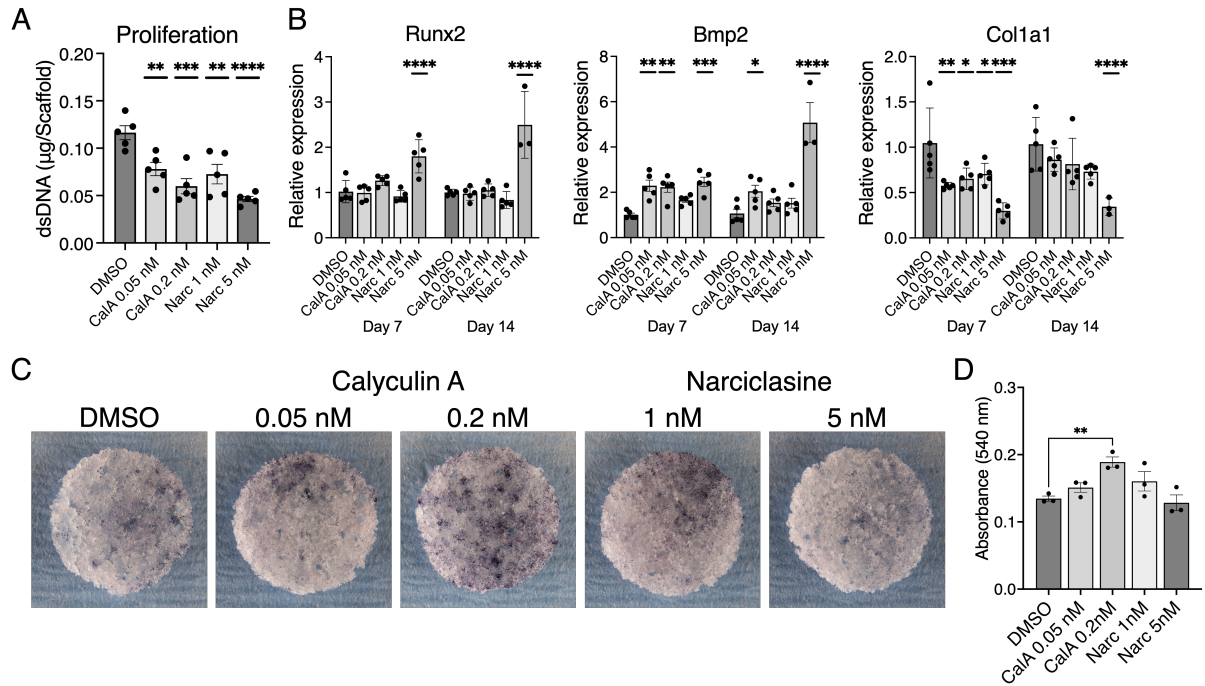
Fig. S3 BMSC Growth and osteogenic properties under pharmacologically triggered actomyosin contraction

BMSC were treated with 0.05 nM and 0.2 nM Calyculin A (CalA) and 1 nM and 5 nM Narciclasine (Narc) (A) Quantification of double-strand DNA (dsDNA) after 7 days of static culture. (B) mRNA expression of putative osteogenic markers after 7 days of static culture. (C, D) Alkaline phosphatase staining and quantification of extracted substrate after 14 days of static culture. * $p<0.05$, ** $p<0.01$, *** $p<0.001$, **** $p<0.0001$.

Table. S1 A set of genes and primers used for the assessment of cytoskeletal rearrangement under perfusion

Gene Symbol	Gene Name	TaqMan Assay ID	Amplicon Length (bp)
Target genes	Actn1	actinin, alpha 1	Rn00667357_m1	66
	Actn3	actinin alpha 3	Rn00591594_m1	88
	Actn4	actinin alpha 4	Rn00581554_m1	69
	Actr2	ARP2 actin-related protein 2 homolog	Rn01434079_m1	83
	Actr3	ARP3 actin-related protein 3 homolog	Rn01753774_m1	99
	Akt1	v-akt murine thymoma viral oncogene homolog 1	Rn00583646_m1	87
	Akt2	v-akt murine thymoma viral oncogene homolog 2	Rn00690900_m1	138
	Akt3	v-akt murine thymoma viral oncogene homolog 3	Rn00442194_m1	71
	Arap1	ArfGAP with RhoGAP domain, ankyrin repeat and PH domain 1	Rn01506749_m1	66
	Arfip2	ADP-ribosylation factor interacting protein 2	Rn01508475_m1	90
	Arhgap5	Rho GTPase activating protein 5	Rn03036858_s1	106
	Arhgap5	Rho GTPase activating protein 5	Rn03036858_s1	106
	Arhgdib	Rho, GDP dissociation inhibitor (GDI) beta	Rn01459333_m1	62
	Arhgef1	Rho guanine nucleotide exchange factor (GEF) 1	Rn00572505_m1	84
	Arhgef11	Rho guanine nucleotide exchange factor (GEF) 11	Rn00576857_m1	67
	Arpc1b	actin related protein 2/3 complex, subunit 1B	Rn00820959_g1	80
	Arpc2	actin related protein 2/3 complex, subunit 2	Rn01400361_m1	62
	Arpc3	actin related protein 2/3 complex, subunit 3	Rn01481651_m1	72
	Arpc4	actin related protein 2/3 complex, subunit 4	Rn01426286_m1	64
	Arpc5	actin related protein 2/3 complex, subunit 5	Rn01759260_m1	93
	Aurka	aurora kinase A	Rn00821847_g1	91
	Aurkb	aurora kinase B	Rn01460656_m1	95
	Aurkc	aurora kinase C	Rn01523742_g1	68
	Baiap2	BAI1-associated protein 2	Rn00589411_m1	97
	Bcar1	breast cancer anti-estrogen resistance 1	Rn00564003_m1	59
	Braf	B-Raf proto-oncogene, serine/threonine kinase	Rn01500563_m1	60
	Cald1	caldesmon 1	Rn00565719_m1	98
	Calm1	calmodulin 1	Rn00821407_g1	82
	Capn2	calpain 2	Rn00567422_m1	83
	Cask	calcium/calmodulin-dependent serine protein kinase	Rn00573365_m1	89
	Cav1	caveolin 1, caveolae protein	Rn00755834_m1	64
	Cav2	caveolin 2	Rn00590969_m1	72
	Cav3	caveolin 3	Rn00755343_m1	64
	Ccna1	cyclin A1	Rn01761351_m1	59
	Ccnb1	cyclin B1	Rn01494177_m1	97
	Ccnb2	cyclin B2	Rn02346769_g1	94
	Cdc42	cell division cycle 42	Rn00696671_m1	75
	Cdc42bpa	CDC42 binding protein kinase alpha	Rn00586620_m1	76
	Cdc42ep2	CDC42 effector protein (Rho GTPase binding) 2	Rn02376973_s1	63
	Cdc42ep3	CDC42 effector protein (Rho GTPase binding) 3	Rn01468719_m1	71
	Cdk5	cyclin-dependent kinase 5	Rn04219635_m1	95
	Cdk5r1	cyclin-dependent kinase 5, regulatory subunit 1 (p35)	Rn02132948_s1	134
	Cfl1	cofilin 1, non-muscle	Rn01501422_g1	77
	Cit	citron rho-interacting serine/threonine kinase	Rn00582449_m1	64
	Clasp1	cytoplasmic linker associated protein 1	Rn01408768_m1	59
	Clasp2	cytoplasmic linker associated protein 2	Rn00586859_m1	70
	Clip1	CAP-GLY domain containing linker protein 1	Rn00582048_m1	77
	Clip2	CAP-GLY domain containing linker protein 2	Rn00573248_m1	77
	Crk	v-crk avian sarcoma virus CT10 oncogene homolog	Rn00467066_m1	86
	Crkl	crk-like protein-like;v-crk avian sarcoma virus CT10 oncogene homolog-like	Rn01753203_m1	94
	Ctnnb1	catenin, beta 1	Rn00584431_g1	86
	Cttn	cortactin	Rn00573209_m1	67
	Cyfip1	cytoplasmic FMR1 interacting protein 1	Rn01409823_m1	59
	Cyfip2	cytoplasmic FMR1 interacting protein 2	Rn01409982_m1	65
	Diaph2	diaphanous-related formin 1	Rn01406955_m1	59
	Diaph1	diaphanous-related formin 1	Rn01406955_m1	59
	Dst	dystonin	Rn02110514_s1	93
	Dstn	destrin;destrin-like 1	Rn01415640_g1	89
	Ezr	ezrin	Rn01526350_m1	87
	Flna	filamin A, alpha	Rn01187530_m1	61
	Flnb	filamin B, beta	Rn01537993_m1	64
	Fnbp1l	formin binding protein 1-like	Rn01523678_m1	58
	Fscn2	fascin actin-bundling protein 2, retinal	Rn01470865_m1	61
	Fyn	FYN proto-oncogene, Src family tyrosine kinase	Rn00562616_m1	105
	Grb2	growth factor receptor bound protein 2	Rn01471333_g1	142
	Gsk3b	glycogen synthase kinase 3 beta	Rn00583429_m1	71
	Gsn	gelsolin	Rn01438922_m1	129
	Hras	Harvey rat sarcoma virus oncogene	Rn01479663_gH	72
	Ilk	integrin-linked kinase	Rn00591471_m1	70
	Iqgap1	IQ motif containing GTPase activating protein 1	Rn01478183_m1	62
	Itga1	integrin, alpha 1	Rn00578564_m1	71
	Itga10	integrin, alpha 10	Rn01533928_m1	73
	Itga11	integrin, alpha 11	Rn01421747_m1	54
	Itga2	integrin, alpha 2	Rn01489315_m1	52
	Itga2b	integrin, alpha 2B	Rn01456695_g1	108
	Itga3	integrin, alpha 3	Rn01751608_m1	61
	Itga4	integrin, alpha 4	Rn01512798_m1	97
	Itga5	integrin, alpha 5	Rn01761831_m1	91
	Itga6	integrin, alpha 6	Rn01512708_m1	53
	Itga7	integrin, alpha 7	Rn01529354_m1	56
	Itga8	integrin, alpha 8	Rn01487205_m1	78
	Itgal	integrin, alpha L	Rn01754645_m1	77
	Itgam	integrin, alpha M	Rn00709342_m1	76
	Itgav	integrin, alpha V	Rn01485633_m1	61
	Itgax	integrin, alpha X	Rn01511082_m1	64
	Itgb1	integrin, beta 1	Rn00566727_m1	81
	Itgb2	integrin, beta 2	Rn01427948_m1	142
	Itgb3	integrin, beta 3	Rn00596601_m1	66
	Itgb4	integrin, beta 4	Rn00566017_m1	66
	Itgb5	integrin, beta 5	Rn01439348_m1	63
	Itgb6	integrin, beta 6	Rn01747277_m1	82
	Limk1	LIM domain kinase 1	Rn00581900_m1	68
	Limk2	LIM domain kinase 2	Rn00577115_m1	60
	Llgl1	lethal giant larvae homolog 1	Rn00596096_m1	59
	Macf1	microtubule-actin crosslinking factor 1	Rn01516936_m1	56
	Map3k11	mitogen-activated protein kinase kinase kinase 11	Rn01502070_m1	149
	Map4	microtubule-associated protein 4	Rn01403680_m1	70
	Map6	microtubule-associated protein 6	Rn00567957_m1	95
	Mapk13	mitogen activated protein kinase 13	Rn00693138_m1	77
	Mapre1	microtubule-associated protein, RP/EB family, member 1	Rn00817431_g1	98
	Mapt	microtubule-associated protein tau	Rn01495715_m1	62
	Mark2	MAP/microtubule affinity-regulating kinase 2	Rn00433039_m1	68
	Mid1	midline 1	Rn00575975_m1	128
	Msn	moesin	Rn01424413_m1	58
	Mylk	myosin light chain kinase	Rn01439252_m1	72
	Mylk2	myosin light chain kinase 2	Rn00679009_m1	59
	Nck1	NCK adaptor protein 1	Rn01447186_m1	115
	Nck2	NCK adaptor protein 2	Rn01438228_m1	100
	Pak1	p21 protein (Cdc42/Rac)-activated kinase 1	Rn00664986_m1	98
	Pak2	p21 protein (Cdc42/Rac)-activated kinase 2	Rn00584005_m1	138
	Pak3	p21 protein (Cdc42/Rac)-activated kinase 3	Rn00693022_m1	72
	Pak4	p21 protein (Cdc42/Rac)-activated kinase 4	Rn01764387_m1	66
	Pak4	p21 protein (Cdc42/Rac)-activated kinase 4	Rn01764387_m1	66
	Parva	parvin, alpha	Rn00571958_m1	66
	Pdpk1	3-phosphoinositide dependent protein kinase-1	Rn00579366_m1	78
	Pfn2	profilin 2;profilin-2-like	Rn00450822_m1	104
	Plekhb2	pleckstrin homology-like domain, family B, member 2	Rn01763372_m1	98
	Pip5k1c	phosphatidylinositol-4-phosphate 5-kinase, type I, gamma	Rn01408490_m1	61
	Plec	plectin	Rn00673737_m1	77
	Ppp1r12b	protein phosphatase 1, regulatory subunit 12B	Rn01490961_m1	67
	Ppp3ca	protein phosphatase 3, catalytic subunit, alpha isozyme	Rn00690508_m1	72
	Ppp3cb	protein phosphatase 3, catalytic subunit, beta isozyme	Rn00566864_m1	138
	Prkca	protein kinase C, alpha	Rn01496145_m1	74
	Prkcb	protein kinase C, beta	Rn00562312_m1	120
	Prkcg	protein kinase C, gamma	Rn00440861_m1	89
	Pten	phosphatase and tensin homolog	Rn00477208_m1	73
	Ptk2	protein tyrosine kinase 2	Rn01505115_m1	81
	Pxn	paxillin	Rn01499294_m1	71
	Rac1	ras-related C3 botulinum toxin substrate 1	Rn01412766_m1	86
	Rac2	ras-related C3 botulinum toxin substrate 2	Rn01504461_g1	57
	Racgap1	rac GTPase-activating protein 1	Rn01761773_m1	62
	Raf1	v-raf-leukemia viral oncogene 1	Rn00465071_m1	88
	Rap1a	RAP1A, member of RAS oncogene family	Rn01533681_g1	139
	Rap1b	RAP1B, member of RAS oncogene family	Rn01509461_gH	108
	Rapgef1	Rap guanine nucleotide exchange factor (GEF) 1	Rn01438718_m1	64
	Rasgrf1	RAS protein-specific guanine nucleotide-releasing factor 1	Rn01447219_m1	54
	Rhoa	ras homolog family member A	Rn04219609_m1	100
	Rock1	Rho-associated coiled-coil containing protein kinase 1	Rn00579490_m1	75
	Rock2	Rho-associated coiled-coil containing protein kinase 2	Rn00564633_m1	73
	Sh3rf1	SH3 domain containing ring finger 1	Rn01535121_m1	78
	Shc1	SHC (Src homology 2 domain containing) transforming protein 1	Rn01458709_g1	131
	Shc2	SHC (Src homology 2 domain containing) transforming protein 2	Rn01171467_m1	63
	Sos1	Son of sevenless homolog 1	Rn01473774_m1	141
	Sos2	Son of sevenless homolog 2	Rn01468822_m1	68
	Src	SRC proto-oncogene, non-receptor tyrosine kinase	Rn00583063_m1	75
	Ssh2	slingshot protein phosphatase 2	Rn01471631_m1	77
	Stmn1	stathmin 1	Rn00691285_g1	137
	Tiam1	T-cell lymphoma invasion and metastasis 1	Rn01477317_m1	61
	Tln1	talin 1	Rn01440247_m1	64
	Tns2	tensin 2	Rn01532783_m1	130
	Tns4	tensin 4	Rn01751085_m1	60
	Vasp	vasodilator-stimulated phosphoprotein	Rn01477032_m1	146
	Vav1	vav 1 guanine nucleotide exchange factor	Rn00562712_m1	69
	Vav2	vav 2 guanine nucleotide exchange factor	Rn01436349_m1	63
	Vcl	vinculin	Rn01755894_m1	63
	Was	Wiskott-Aldrich syndrome	Rn01528309_m1	82
	Wasf1	WAS protein family, member 1	Rn01754124_m1	72
	Wasl	Wiskott-Aldrich syndrome-like	Rn01501122_m1	63
	Zyx	zyxin	Rn01501253_m1	57

Table. S2 A set of genes and primers used for the assessment of osteogenic profile under perfusion

	Gene Symbol	Gene Name	TaqMan Assay ID	Amplicon Length (bp)
Target genes	Ahsg	alpha-2-HS-glycoprotein	Rn00563700_m1	113
	Alpl	alkaline phosphatase	Rn01516028_m1	68
	Anxa5	annexin A5	Rn00565571_m1	115
	Bglap	bone gamma-carboxyglutamate (gla) protein	Rn01455285_g1	81
	Bgn	biglycan	Rn00567229_m1	76
	Bmp1	bone morphogenetic protein 1	Rn01466016_m1	75
	Bmp2	bone morphogenetic protein 2	Rn00567818_m1	126
	Bmp3	bone morphogenetic protein 3	Rn00690955_mH	60
	Bmp4	bone morphogenetic protein 4	Rn00432087_m1	61
	Bmp5	bone morphogenetic protein 5	Rn01447676_m1	78
	Bmp6	bone morphogenetic protein 6	Rn00432095_m1	122
	Bmp7	bone morphogenetic protein 7	Rn01528889_m1	65
	Bmpr1a	bone morphogenetic protein receptor, type IA	Rn01450292_g1	82
	Bmpr1b	bone morphogenetic protein receptor, type IB	Rn01748421_m1	67
	Cdh11	cadherin 11	Rn01536913_m1	61
	Col10a1	collagen, type X, alpha 1	Rn01408030_m1	80
	Col11a1	collagen, type XI, alpha 1	Rn01523309_m1	54
	Col12a1	collagen, type XII, alpha 1	Rn01521220_m1	57
	Col14a1	collagen, type XIV, alpha 1	Rn01502357_m1	57
	Col1a1	collagen, type I, alpha 1	Rn01463848_m1	115
	Col1a2	collagen, type I, alpha 2	Rn01526721_m1	96
	Col2a1	collagen, type II, alpha 1	Rn01637087_m1	97
	Col3a1	collagen, type III, alpha 1	Rn01437681_m1	71
	Col4a1	collagen, type IV, alpha 1	Rn01482927_m1	69
	Col4a2	collagen, type IV, alpha 2	Rn01482133_m1	53
	Col5a1	collagen, type V, alpha 1	Rn00593170_m1	61
	Col6a1	collagen, type VI, alpha 1	Rn01429556_m1	67
	Col6a2	collagen, type VI, alpha 2	Rn01429497_m1	77
	Col7a1	collagen, type VII, alpha 1	Rn01544829_m1	60
	Comp	cartilage oligomeric matrix protein	Rn00563255_m1	87
	Csf2	colony stimulating factor 2	Rn01456851_m1	127
	Csf3	colony stimulating factor 3	Rn00567344_m1	95
	Ctsk	cathepsin K	Rn00580723_m1	69
	Cyr61	cysteine-rich, angiogenic inducer, 61	Rn00580055_m1	113
	Dmp1	dentin matrix acidic phosphoprotein 1	Rn01450122_m1	77
	Egf	epidermal growth factor	Rn00563336_m1	93
	Fgf1	fibroblast growth factor 1	Rn00689153_m1	78
	Fgf2	fibroblast growth factor 2	Rn00570809_m1	63
	Fgf3	fibroblast growth factor 3	Rn00590754_m1	60
	Fgfr1	Fibroblast growth factor receptor 1	Rn00577234_m1	78
	Fgfr2	fibroblast growth factor receptor 2	Rn01269940_m1	87
	Flt1	FMS-related tyrosine kinase 1	Rn00570815_m1	60
	Fn1	fibronectin 1	Rn00569575_m1	97
	Gdf10	growth differentiation factor 10	Rn00666937_m1	105
	Ibsp	integrin-binding sialoprotein	Rn00561414_m1	138
	Icam1	intercellular adhesion molecule 1	Rn00564227_m1	61
	Igf1	insulin-like growth factor 1	Rn00710306_m1	69
	Igf1r	insulin-like growth factor 1 receptor	Rn00583837_m1	58
	Itga2	integrin, alpha 2	Rn01489315_m1	52
	Itga3	integrin, alpha 3	Rn01751608_m1	61
	Itgb1	integrin, beta 1	Rn00566727_m1	81
	Mmp10	matrix metallopeptidase 10	Rn00591678_m1	79
	Mmp2	matrix metallopeptidase 2	Rn01538170_m1	63
	Mmp8	matrix metallopeptidase 8	Rn00573646_m1	92
	Mmp9	matrix metallopeptidase 9	Rn00579162_m1	72
	Msx1	msh homeobox 1	Rn00667535_m1	83
	Nfkb1	nuclear Factor Kappa B Subunit 1	Rn01399583_m1	63
	Pdgfa	platelet-derived growth factor alpha polypeptide	Rn00709363_m1	62
	Phex	phosphate regulating endopeptidase homolog, X-linked	Rn00448130_m1	95
	Runx2	runt-related transcription factor 2	Rn01512298_m1	86
	Scarb1	scavenger receptor class B, member 1	Rn00580588_m1	75
	Serpinh1	Serpin Family H Member 1	Rn00567777_m1	76
	Smad1	SMAD family member 1	Rn00565555_m1	79
	Smad2	SMAD family member 2	Rn00569900_m1	67
	Smad3	SMAD family member 3	Rn00565331_m1	94
	Smad4	SMAD family member 4	Rn00570593_m1	101
	Sost	sclerostin	Rn00577971_m1	81
	Sox9	SRY (sex determining region Y)-box 9	Rn01751069_mH	60
	Sp7	Sp7 transcription factor	Rn01761789_m1	107
	Spp1	secreted phosphoprotein 1	Rn00681031_m1	73
	Tfip11	tuftelin interacting protein 11	Rn01481123_m1	125
	Tgfb1	transforming growth factor, beta 1	Rn00572010_m1	65
	Tgfb2	transforming growth factor, beta 2	Rn00579674_m1	95
	Tgfb3	transforming growth factor, beta 3	Rn00565937_m1	61
	Tgfbr1	transforming growth factor, beta receptor 1	Rn00562811_m1	86
	Tgfbr2	transforming growth factor, beta receptor 2	Rn00579682_m1	74
	Tgfbr3	transforming growth factor, beta receptor 3	Rn00568482_m1	89
	Tnf	tumor necrosis factor	Rn00562055_m1	82
	Tuft1	tuftelin 1	Rn01762781_m1	68
	Twist1	twist family bHLH transcription factor 1	Rn00585470_s1	71
	Vcam1	vascular cell adhesion molecule 1	Rn00563627_m1	90
	Vdr	vitamin D receptor	Rn00690616_m1	63
	Vegfa	vascular endothelial growth factor A	Rn01511601_m1	69
	Vegfb	vascular endothelial growth factor B	Rn01454585_g1	68

Table. S3 A set of genes and primers used as an endogeneous control

	Gene Symbol	Gene Name	TaqMan Assay ID	Amplicon Length (bp)
Endogenous control	18S	Eukaryotic 18S rRNA	Hs99999901_s1	187
	B2m	beta-2 microglobulin	Rn00560865_m1	58
	Gapdh	glyceraldehyde-3-phosphate dehydrogenase	Rn99999916_s1	87
	Gusb	glucuronidase, beta	Rn00566655_m1	63
	Hmbs	hydroxymethylbilane synthase	Rn00565886_m1	99
	Hprt1	hypoxanthine phosphoribosyltransferase 1	Rn01527840_m1	64
	Pgk1	phosphoglycerate kinase 1	Rn00821429_g1	84
	Rplp0	ribosomal protein, large, P0	Rn00821065_g1	97
	Rplp2	ribosomal protein, large P2	Rn01479927_g1	130